

# Fast Ewald Summation using Prolate Spheroidal Wave Functions

Erik Boström\*, Anna-Karin Tornberg† Ludvig af Klinteberg\*

## Abstract

Fast Ewald summation efficiently evaluates Coulomb interactions and is widely used in molecular dynamics simulations. It is based on a split into a short-range and a long-range part, where evaluation of the latter is accelerated using the fast Fourier transform (FFT). The accuracy and computational cost depend critically on the mollifier in the Ewald split and the window function used in the spreading and interpolation steps that enable the use of the FFT. The first prolate spheroidal wavefunction (PSWF) has optimal concentration in real and Fourier space simultaneously, and is used when defining both a mollifier and a window function. We provide a complete description of the method and derive rigorous error estimates. In addition, we obtain closed-form approximations of the Fourier truncation and aliasing errors, yielding explicit parameter choices for the achieved error to closely match the prescribed tolerance. Numerical experiments confirm the analysis: PSWF-based Ewald summation achieves a given accuracy with significantly fewer Fourier modes and smaller window supports than Gaussian- and B-spline-based approaches, providing a superior alternative to existing Ewald methods for particle simulations.

**Key words:** Ewald summation, prolate spheroidal wavefunction, nonuniform fast Fourier transform, fast algorithms, particle methods

**AMS subject classifications:** 31B10, 41A30, 65T50, 65E05, 65Y20

## 1 Introduction

Long-range interactions such as Coulomb and Stokes potentials arising in particle-based systems are central to molecular dynamics, fluid dynamics, and wave propagation. A major computational challenge is that direct evaluation of such interactions scales quadratically with the number of particles. Ewald summation, introduced in 1921 [12] reduces this cost and has since become a standard tool in large-scale simulations.

In Ewald's original formulation, the three-dimensional Laplace kernel  $G(r) = 1/r$  ( $r = |\mathbf{x}|$ ,  $\mathbf{x} \in \mathbb{R}^3$ ) is decomposed into a mollified kernel  $M(r)$  and a residual kernel  $R(r)$  according to

$$\frac{1}{r} = M(r) + R(r) := \frac{\text{erf}(r/\sigma)}{r} + \frac{\text{erfc}(r/\sigma)}{r}, \quad (1)$$

---

\*Division of Mathematics and Physics, Mälardalen University, 72123 Västerås, Sweden  
 $(\{erik.bostrom, ludvig.af.klinteberg\}@mdu.se)$

†Department of Mathematics, KTH Royal Institute of Technology, 10044 Stockholm, Sweden  
 $(akto@kth.se)$

where  $\text{erf}(x) = \frac{2}{\sqrt{\pi}} \int_0^x e^{-t^2} dt$  and  $\text{erfc}(x) = 1 - \text{erf}(x)$  are the error and complementary error functions. The parameter  $\sigma > 0$  is a width-parameter of the mollification that controls the decay of both terms. In the original Ewald-split (1), the mollified kernel  $M$  is the convolution of  $G$  with a Gaussian  $\frac{1}{\sqrt{\pi}\sigma} e^{-r^2/\sigma^2}$ , while the residual is  $R = G - M$ . Because a Gaussian is not compactly supported,  $R$  must be truncated numerically outside a cutoff radius  $r_c > 0$ , with truncation error controlled by a numerical tolerance that is typically denoted by  $\varepsilon$ .

The Ewald split enables efficient evaluation of the potential  $\phi: \mathbb{R}^3 \rightarrow \mathbb{R}$  at the particle locations  $\{\mathbf{x}_j\}_{j=1}^n$  in a triply periodic domain  $\Omega = [0, L]^3$  (cubic for clarity of presentation; the method extends directly to general periodic lattices). Using (1), it can be written as

$$\phi(\mathbf{x}_i) = \sum_{\mathbf{r} \in \mathbb{Z}^3} \sum_{j=1}^n G(|\mathbf{x}_i - \mathbf{x}_j + L\mathbf{r}|) \rho_j, \quad (2)$$

$$\begin{aligned} &= \frac{1}{L^3} \sum_{\mathbf{k} \neq \mathbf{0}} \hat{M}(\mathbf{k}) \sum_{j=1}^n \rho_j e^{-\frac{2\pi}{L} i \mathbf{k} \cdot (\mathbf{x}_i - \mathbf{x}_j)} - \lim_{r \rightarrow 0} M(r) \rho_i \\ &+ \sum_{\mathbf{r} \in \mathbb{Z}^3} \sum_{j=1}^n R(|\mathbf{x}_i - \mathbf{x}_j + L\mathbf{r}|) \rho_j, \quad i = 1, \dots, n, \end{aligned} \quad (3)$$

where  $\{\rho_j\}_{j=1}^n$  are particle strengths (e.g., charges),  $\mathbf{r} \in \mathbb{Z}^3$  indexes the periodic images, and the prime indicates that the self-interaction ( $i = j, \mathbf{r} = 0$ ) is omitted. The Ewald split (1) makes the otherwise conditionally convergent sum (2) convergent provided that the charge-neutrality condition  $\sum_{j=1}^n \rho_j = 0$  holds. In (3), the mollified part  $M$  is evaluated in Fourier space, where  $\hat{M}(\mathbf{k})$  decays rapidly, while the residual  $R$  captures local interactions within a cutoff radius  $r_c$ . This reduces the cost of evaluating  $\phi$  from  $\mathcal{O}(n^2)$  to  $\mathcal{O}(n^{3/2})$  for close to randomly uniform particle distributions [15].

Several fast Ewald variants accelerate the Fourier-space sum further to  $\mathcal{O}(n \log n)$  using the fast Fourier transform (FFT) [7]. These include the Particle Mesh Ewald (PME) [8], Smooth Particle Mesh Ewald (SPME) [11], Particle–Particle–Particle–Mesh Ewald (PPPM or P<sup>3</sup>M) [15], the Spectral Ewald (SE) [2, 20, 28], and the Particle–Particle NFFT Ewald (P<sup>2</sup>NFFT) method [16, 22]. These schemes spread particle data onto a uniform grid using a localized window function, apply the FFT, scale in Fourier space, and interpolate back. The accuracy and efficiency therefore depend on two distinct choices of functions: (i) the mollifier used in the Ewald split, and (ii) the window function used in spreading and interpolation. Both influence the spectral decay and thus the number of Fourier modes and grid points required for a target accuracy. Classical methods differ mainly in these choices: PME, SPME, and P<sup>3</sup>M employ low-order B-splines as window functions, while SE and P<sup>2</sup>NFFT use Gaussians or various types of approximations to the first prolate spheroidal wavefunction.

The first prolate spheroidal wavefunction of order zero (PSWF), studied extensively by Slepian and collaborators [30, 31] and in [23, 24], is optimally concentrated in both real and Fourier space. This makes it attractive both as a mollifier (for splitting) and as a window function (for spreading/interpolation), though in principle different PSWFs with different parameters may be used for the two roles. Historically, the absence of a closed form limited practical use, and approximations such as the Kaiser–Bessel and exponential of semicircle functions were employed instead [5, 18], including in SE and P<sup>2</sup>NFFT implementations [22, 28]. With modern evaluation algorithms [23] and polynomial approximations [5], PSWFs have become computationally practical.

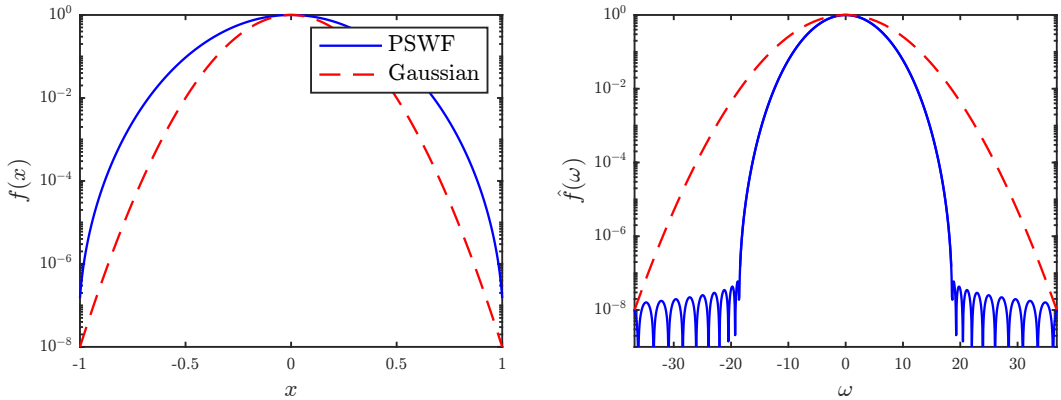


**Figure 1:** Comparison of the Gaussian and the first PSWF of order zero in real space (left) and Fourier space (right). For equal effective support, the PSWF mollifier requires roughly half as many Fourier modes to achieve the same accuracy.

Until recently, PSWFs have primarily been considered as window functions in fast Ewald summation. However, employing them also as mollifiers in the Ewald split yields further advantages, reducing the number of required Fourier modes by around a factor of two in each dimension. Figure 1 illustrates this effect by comparing the decay of the PSWF and Gaussian functions.

The idea of using PSWFs for kernel splitting was first introduced in the Dual-split Multilevel Kernel (DMK) framework [17]. The PSWF split and the DMK algorithm have since also been applied to Stokes potentials [1]. While the DMK framework established the basic concept, a complete mathematical description of PSWF-based Ewald methods is still lacking.

In this paper, we provide such a description, incorporating the first PSWF of order zero both as a mollifier and a window function, with distinct parameters for the two roles. Our main contributions are:

- Explicit definitions of PSWF-based mollifiers and PSWF-based window functions, integrated consistently within the Ewald method.
- Sharp error bounds for both splitting and windowing, with simplified closed-form approximations for practical use.
- Guidelines for parameter selection for the Fourier sum, enabling predictive accuracy control without ad-hoc tuning.
- Systematic comparisons with Gaussian- and B-spline-based methods, demonstrating that PSWF-based approaches achieve equal accuracy with fewer Fourier modes and smaller window supports.

The resulting method is optimal with respect to computational complexity, due to the minimal support of the PSWF. While our analysis focuses on the triply periodic electrostatic potential, it extends naturally to other periodicities and kernels, including Stokes flow [2,3].

Recent work by Liang et al. [19] has emphasized high-performance implementation and benchmarking. Taken together, the results presented here and those of Liang et al. highlight both the theoretical foundations and the practical advantages of PSWF-based Ewald summation.

The remainder of the paper is organized as follows. Section 2 introduces mathematical preliminaries. Section 3 reviews the direct and fast Ewald summation algorithms. Section 4 presents the PSWF-based method. Section 5 provides rigorous error analysis. Section 6 discusses parameter selection. Section 7 reports numerical experiments, and Section 8 concludes the paper.

## 2 Mathematical preliminaries

This section introduces notation and the fundamental concepts used throughout the paper.

### 2.1 Basic definitions and notation

We consider the periodic box  $\Omega = \mathbb{R}^3/(L\mathbb{Z}^3) \simeq [0, L)^3$  with side length  $L$  and volume  $V = L^3$ . Particle locations are  $\{\mathbf{x}_j\}_{j=1}^n \subset \Omega$  with associated strengths  $\{\rho_j\}_{j=1}^n$ . We write  $r = |\mathbf{x}|$ .

Fourier-space variables are  $\mathbf{k} \in \mathbb{Z}^3$  and  $\boldsymbol{\omega} := (2\pi/L)\mathbf{k} \in \mathbb{R}^3$  with  $\omega = |\boldsymbol{\omega}|$ . For a function  $f(\mathbf{x})$ , its Fourier transform is  $\hat{f}(\boldsymbol{\omega})$  (or  $\hat{f}(\mathbf{k})$  when the scaling is clear), Fourier-series coefficients are  $c_{\mathbf{k}}(f)$ , and discrete Fourier transform coefficients are denoted  $\hat{f}_{\mathbf{k}} \approx c_{\mathbf{k}}(f)$ . Radially symmetric functions are written  $f(r)$  with  $r = |\mathbf{x}|$ .

For a cubic bandwidth  $\mathbf{m} = (m, m, m)$  define

$$\mathcal{I}_m := \begin{cases} \{-m/2, \dots, m/2 - 1\}, & m \text{ even}, \\ \{-(m-1)/2, \dots, (m-1)/2\}, & m \text{ odd}, \end{cases} \quad \mathcal{I}_{\mathbf{m}} := \mathcal{I}_m^3, \quad |\mathcal{I}_{\mathbf{m}}| = m^3. \quad (4)$$

Define  $K_{\max} := \lfloor m/2 \rfloor$  and  $\omega_{\max} := (2\pi/L)K_{\max}$ .

### 2.2 A fundamental lemma for Laplacian kernel splitting

The next identity links a one-dimensional function to its three-dimensional convolution with the Laplace kernel  $G(\mathbf{x}) = 1/|\mathbf{x}|$ .

**Lemma 1.** *Let  $f \in L^1(\mathbb{R})$  be even and non-negative, with Fourier transform  $\hat{f}$ . Define the radial function  $g: \mathbb{R}^3 \rightarrow \mathbb{R}$  by*

$$g(\mathbf{x}) := \frac{2}{|\mathbf{x}|} \int_0^{|\mathbf{x}|} f(u) du, \quad \mathbf{x} \neq \mathbf{0}, \quad (5)$$

with  $g(\mathbf{0})$  defined by continuity. Then

$$\hat{g}(\boldsymbol{\omega}) = \frac{4\pi}{|\boldsymbol{\omega}|^2} \hat{f}(|\boldsymbol{\omega}|). \quad (6)$$

**Remark 1** (Radial extension). *Let  $\eta: \mathbb{R}^3 \rightarrow \mathbb{R}$  be the radial extension of  $f$  (see Appendix C.1), i.e.  $\hat{\eta}(\boldsymbol{\omega}) = \hat{f}(|\boldsymbol{\omega}|)$ . Thus  $\hat{g}(\boldsymbol{\omega}) = \hat{G}(\boldsymbol{\omega}) \hat{\eta}(\boldsymbol{\omega})$  with  $\hat{G}(\boldsymbol{\omega}) = 4\pi/|\boldsymbol{\omega}|^2$ , i.e.  $g = G * \eta$ .*

A proof of Lemma 1 using spherical coordinates and integration by parts is given in Appendix A.3 of [17].

### 2.3 Numerical mollifiers for the Laplacian kernel

We call an even and non-negative function  $\gamma_\sigma \in L^1(\mathbb{R})$  with width parameter  $\sigma > 0$  a *numerical mollifier* (or simply a *mollifier*) if

$$\int_{\mathbb{R}} \gamma_\sigma(x) dx = 1, \quad (7)$$

and

$$|\gamma_\sigma(x)| \leq \delta \quad \text{for all } |x| \geq \sigma, \quad (8)$$

where  $\delta > 0$  is a prescribed tolerance controlling the tail of  $\gamma_\sigma$ .

By Lemma 1, the mollified Laplace kernel and its Fourier transform are

$$M(\mathbf{x}) := (G * \eta_\sigma)(\mathbf{x}) = \frac{2 \int_0^{|\mathbf{x}|} \gamma_\sigma(u) du}{|\mathbf{x}|}, \quad (9)$$

$$\hat{M}(\boldsymbol{\omega}) = \hat{G}(\boldsymbol{\omega}) \hat{\eta}_\sigma(\boldsymbol{\omega}) = \frac{4\pi}{|\boldsymbol{\omega}|^2} \hat{\gamma}_\sigma(|\boldsymbol{\omega}|). \quad (10)$$

Here  $\eta_\sigma$  is the radial extension of  $\gamma_\sigma$ . In Ewald summation,  $M$  is the *mollified kernel* and  $R := G - M$  the *residual kernel*, with  $\sigma$  chosen so that  $|R(r_c)| \lesssim \varepsilon$  at the cutoff radius  $r_c$ .

**Remark 2.** *In previous work, e.g. [20], the residual kernel  $R$  is not compactly supported, and the parameters  $\sigma$  and  $k_{\max}$  are chosen so that the resulting error matches approximate error models, rather than by imposing a condition such as  $|R(r_c)| \lesssim \varepsilon$ . The condition  $|R(r_c)| \lesssim \varepsilon$  nevertheless provides a sufficient starting point for subsequent fine-tuning of the parameters; see also [19]. Due to the construction of the mollifier, we can instead achieve  $R(r_c) = 0$  (as shown in Section 4), which eliminates truncation errors in the residual kernel and makes the parameter selection process easier and entirely determined by the Fourier-space sum.*

**Example 1** (Gaussian mollifier). The 1D Gaussian

$$g(x) = \frac{1}{\sqrt{\pi}} e^{-x^2}, \quad \hat{g}(\omega) = e^{-\omega^2/4}, \quad (11)$$

scaled by a width parameter  $\sigma > 0$ ,

$$g_\sigma(x) = \frac{1}{\sqrt{\pi}\sigma} e^{-x^2/\sigma^2}, \quad \hat{g}_\sigma(\omega) = e^{-\sigma^2\omega^2/4}, \quad (12)$$

is a mollifier in the sense of the definition above. It yields the classical Gaussian Ewald split

$$M(\mathbf{x}) = \frac{\operatorname{erf}(|\mathbf{x}|/\sigma)}{|\mathbf{x}|}, \quad \hat{M}(\boldsymbol{\omega}) = \frac{4\pi}{|\boldsymbol{\omega}|^2} e^{-\sigma^2|\boldsymbol{\omega}|^2/4}, \quad (13)$$

with residual

$$R(|\mathbf{x}|) = \frac{\operatorname{erfc}(|\mathbf{x}|/\sigma)}{|\mathbf{x}|}. \quad (14)$$

Since  $\operatorname{erfc}(|\mathbf{x}|/\sigma)$  decays exponentially, the residual kernel becomes smaller than  $\varepsilon$  for  $|\mathbf{x}| \gtrsim r_c$ , provided that

$$(r_c/\sigma)^2 \gtrsim \log(1/\varepsilon). \quad (15)$$

## 2.4 Window functions, periodization and Fourier coefficients

We define a *window function* as a real and even function  $\varphi \in L^2(\mathbb{R}^3)$  for which both  $\varphi$  and  $\hat{\varphi}$  are strongly localized near zero, enabling compact truncation in real space and rapid spectral decay.

If a window function without compact support is used, it can be truncated. We define its truncation by

$$\varphi_t(\mathbf{x}) := \begin{cases} \varphi(\mathbf{x}), & \mathbf{x} \in [-\alpha, \alpha]^3, \\ 0, & \mathbf{x} \notin [-\alpha, \alpha]^3. \end{cases} \quad (16)$$

On the periodic domain  $\Omega$ , a periodized window function  $\tilde{\varphi}$  is employed. More generally, for any  $f$  on  $\mathbb{R}^3$  we define the periodization  $\tilde{f}$  on  $\Omega$  by

$$\tilde{f}(\mathbf{x}) := \sum_{\mathbf{r} \in \mathbb{Z}^3} f(\mathbf{x} + L\mathbf{r}), \quad (17)$$

which admits the Fourier series

$$\tilde{f}(\mathbf{x}) = \sum_{\mathbf{k} \in \mathbb{Z}^3} c_{\mathbf{k}}(\tilde{f}) e^{\frac{2\pi}{L} i \mathbf{k} \cdot \mathbf{x}}, \quad (18)$$

with coefficients (see Appendix C.2 for the derivation)

$$c_{\mathbf{k}}(\tilde{f}) = \frac{1}{V} \int_{\Omega} \tilde{f}(\mathbf{x}) e^{-\frac{2\pi}{L} i \mathbf{k} \cdot \mathbf{x}} d\mathbf{x} = \frac{1}{V} \hat{f}\left(\frac{2\pi}{L} \mathbf{k}\right). \quad (19)$$

Hence

$$\tilde{f}(\mathbf{x}) = \frac{1}{V} \sum_{\mathbf{k} \in \mathbb{Z}^3} \hat{f}\left(\frac{2\pi}{L} \mathbf{k}\right) e^{\frac{2\pi}{L} i \mathbf{k} \cdot \mathbf{x}}. \quad (20)$$

**Remark 3.** We distinguish Fourier series coefficients from discrete Fourier transform (DFT) coefficients. For  $f \in L^2(\Omega)$  sampled on an  $m^3$  uniform grid, the DFT produces  $\hat{f}_{\mathbf{k}}$  for  $\mathbf{k} \in \mathcal{I}_m$ , related to  $c_{\mathbf{k}}(f)$  by the aliasing identity [25]

$$\hat{f}_{\mathbf{k}} = \sum_{\mathbf{r} \in \mathbb{Z}^3} c_{\mathbf{k} + m\mathbf{r}}(f). \quad (21)$$

## 2.5 Prolate Spheroidal Wave Functions

The *prolate spheroidal wave functions* (PSWFs),  $\{\psi_j^c\}_{j=0}^{\infty}$ , arise as eigenfunctions of the integral operator

$$F_c[f](s) := \int_{-1}^1 f(t) e^{icst} dt, \quad s \in [-1, 1], \quad (22)$$

where  $c > 0$  is the *bandlimit*. They satisfy

$$\lambda_j \psi_j^c(s) = \int_{-1}^1 \psi_j^c(t) e^{icst} dt, \quad (23)$$

with eigenvalues ordered by decreasing modulus

$$\sqrt{\frac{2\pi}{c}} > |\lambda_0(c)| > |\lambda_1(c)| > \dots > 0. \quad (24)$$

The functions  $\psi_j^c$  are real, orthonormal in  $L^2([-1, 1])$ , and alternate parity with  $j$  [24].

Among bandlimited functions, the first PSWF  $\psi_0^c$  ( $j = 0$ ) maximizes spectral concentration:

**Theorem 1** ([24, Thm. 3.53]). Let  $f \in L^2([-1, 1])$  with  $\|f\|_{L^2([-1,1])} = 1$  and  $c > 0$ . Define  $g$  by

$$g(s) = \int_{-1}^1 f(t) e^{icst} dt, \quad s \in \mathbb{R}. \quad (25)$$

Then

$$\|g\|_{L^2(\mathbb{R})}^2 = \frac{2\pi}{c}, \quad \|g\|_{L^2([-1,1])}^2 \leq |\lambda_0(c)|^2, \quad (26)$$

with equality for  $f = \psi_0^c$ .

Thus only  $\psi_0^c$  is needed in the present work. Its Fourier transform satisfies a simple relation:

**Lemma 2.** Let  $\hat{\psi}_0^c(\omega) = \int_{-1}^1 \psi_0^c(x) e^{i\omega x} dx$ . For  $\omega \in [-c, c]$ ,

$$\hat{\psi}_0^c(\omega) = \lambda_0 \psi_0^c(\omega/c). \quad (27)$$

For computation,  $\psi_0^c$  can be obtained from its Legendre expansion and a tridiagonal eigenproblem derived from the differential equation [23]

$$\frac{d}{dx} \left( (1-x^2) \frac{d\psi_0^c}{dx} \right) + (\chi_0 - c^2 x^2) \psi_0^c = 0, \quad (28)$$

with details given in Appendix B.

### 3 Ewald summation

Before presenting the PSWF-based implementation, we briefly review the classical Ewald summation and its components. We then summarize the general fast Ewald algorithm, in which the PSWF will serve as both mollifier and window.

#### 3.1 Ewald summation for triply periodic problems

Recall, the *Ewald split* of a radial kernel  $G: \mathbb{R}^3 \rightarrow \mathbb{R}$  is

$$G(r) = M(r) + R(r), \quad (29)$$

where  $M$  and  $R$  are the mollified and residual kernels, respectively. Periodizing this decomposition on  $\Omega$  gives

$$\sum_{\mathbf{r} \in \mathbb{Z}^3} G(|\mathbf{x} + L\mathbf{r}|) = \sum_{\mathbf{r} \in \mathbb{Z}^3} M(|\mathbf{x} + L\mathbf{r}|) + \sum_{\mathbf{r} \in \mathbb{Z}^3} R(|\mathbf{x} + L\mathbf{r}|). \quad (30)$$

Using this, the *Ewald sum* for the triply periodic potential  $\phi$  evaluated at particle locations  $\mathbf{x}_i \in \Omega$  ( $i = 1, \dots, n$ ) is

$$\phi_i := \phi(\mathbf{x}_i) = \sum_{\mathbf{r} \in \mathbb{Z}^3} \sum_{j=1}^n G(|\mathbf{x}_i - \mathbf{x}_j + L\mathbf{r}|) \rho_j = \phi_i^{\text{local}} + \phi_i^{\text{far}} + \phi_i^{\text{self}}, \quad (31)$$

where

$$\phi_i^{\text{local}} := \sum_{\mathbf{r} \in \mathbb{Z}^3} \sum_{j=1}^n {}' R(|\mathbf{x}_i - \mathbf{x}_j + L\mathbf{r}|) \rho_j, \quad (32)$$

$$\phi_i^{\text{far}} := \sum_{\mathbf{r} \in \mathbb{Z}^3} \sum_{j=1}^n M(|\mathbf{x}_i - \mathbf{x}_j + L\mathbf{r}|) \rho_j, \quad (33)$$

$$\phi_i^{\text{self}} := - \lim_{|\mathbf{x}| \rightarrow 0} M(|\mathbf{x}|) \rho_i. \quad (34)$$

The self-term removes the self-interaction at  $\mathbf{x}_i = \mathbf{x}_j$  that would otherwise be included in  $\phi_i^{\text{far}}$ .

For  $G(r) = 1/r$ , the residual kernel  $R$  decays rapidly in real space. Moreover,  $\hat{M}(\omega) = 4\pi \hat{\gamma}_\sigma(|\omega|)/|\omega|^2$ , and if  $\gamma_\sigma$  is compactly supported and sufficiently smooth, then by the Paley–Wiener theorem  $\hat{M}$  decays superalgebraically, enabling efficient evaluation of  $\phi_i$  [25].

**Remark 4.** *Given that  $\phi_i$  denotes the electrostatic potential at  $\mathbf{x}_i$ , the total electrostatic energy is*

$$E = \frac{1}{2} \sum_{i=1}^n \rho_i \phi_i = \frac{1}{2} \sum_{\mathbf{r} \in \mathbb{Z}^3} \sum_{i=1}^n \sum_{j=1}^n {}' \rho_i \rho_j G(|\mathbf{x}_i - \mathbf{x}_j + L\mathbf{r}|), \quad (35)$$

and the force acting on particle  $i$  is given by

$$\mathbf{F}_i = -\rho_i \nabla \phi_i = - \sum_{\mathbf{r} \in \mathbb{Z}^3} \sum_{j=1}^n {}' \rho_i \rho_j \nabla G(|\mathbf{x}_i - \mathbf{x}_j + L\mathbf{r}|). \quad (36)$$

The practical evaluation of the force within the proposed Ewald method, including the corresponding real- and Fourier-space contributions, is discussed in detail in Remark 8 (see in particular (65)).

### 3.1.1 Computing the real-space sum

The real-space sum  $\phi_i^{\text{local}}$  is computationally efficient because the kernel  $R$  decays rapidly. If  $R$  is not compactly supported, it is truncated at a cutoff radius  $r_c$  such that  $|R(r_c)| \lesssim \varepsilon$ , ensuring that the truncation error is of the same order of magnitude as the prescribed tolerance (cf. Example 1). Consequently, only particles within a distance  $r_c$  of  $\mathbf{x}_i$  are included in the computation. For uniform particle distributions, let  $n_{r_c}$  denote the number of particles within distance  $r_c$  of each  $\mathbf{x}_i$ . Then, when, e.g., neighbor or cell lists are employed [15], the total computational cost of this evaluation scales as  $\mathcal{O}(n_{r_c} n)$ .

### 3.1.2 Direct computation of the Fourier-space sum

Using (19), the far-field component (33) is approximated by the truncated Fourier representation

$$\phi_i^{\text{far}} \approx \frac{1}{V} \sum_{\mathbf{k} \in \mathcal{I}_m \setminus \{\mathbf{0}\}} \hat{M}(\mathbf{k}) \hat{\rho}(\mathbf{k}) e^{-\frac{2\pi i}{L} \mathbf{k} \cdot \mathbf{x}_i}, \quad i = 1, \dots, n. \quad (37)$$

Here,

$$\hat{M}(\mathbf{k}) = \hat{G}(|\boldsymbol{\omega}(\mathbf{k})|) \hat{\gamma}_\sigma(|\boldsymbol{\omega}(\mathbf{k})|) = \frac{L^2}{\pi|\mathbf{k}|^2} \hat{\gamma}_\sigma(|\boldsymbol{\omega}(\mathbf{k})|), \quad \boldsymbol{\omega}(\mathbf{k}) := \frac{2\pi}{L}\mathbf{k}, \quad (38)$$

and the so-called *structure factor* is defined as

$$\hat{\rho}(\mathbf{k}) := \sum_{j=1}^n \rho_j e^{\frac{2\pi}{L}i\mathbf{k}\cdot\mathbf{x}_j}, \quad \rho(\mathbf{x}) := \sum_{j=1}^n \rho_j \delta(\mathbf{x} - \mathbf{x}_j). \quad (39)$$

where  $\delta$  is the 3D Dirac delta distribution. Under the charge neutrality condition, the  $\mathbf{k} = \mathbf{0}$  mode vanishes and is therefore omitted from the sum.

Let  $\boldsymbol{\phi}^{\text{far}} = (\phi_j^{\text{far}})_{j=1}^n$  and  $\boldsymbol{\rho} = (\rho_j)_{j=1}^n$  be the length- $n$  vector of the potential and the source strengths at each  $\mathbf{x}_j$ , let  $\mathbf{U} \in \mathbb{C}^{|\mathcal{I}_m| \times n}$  be the nonuniform Fourier matrix with entries  $\mathbf{U}_{\ell j} = e^{\frac{2\pi}{L}i\mathbf{k}_\ell \cdot \mathbf{x}_j}$ , and let  $\mathbf{D} = \text{diag}(V^{-1}\hat{M}(\mathbf{k}_\ell))$ , with the  $\mathbf{k} = \mathbf{0}$  entry set to zero. Then we can write (37) in matrix form as

$$\boldsymbol{\phi}^{\text{far}} \approx \mathbf{U}^* \mathbf{D} \mathbf{U} \boldsymbol{\rho}. \quad (40)$$

Direct evaluation of (40) using full Fourier matrices is clearly  $\mathcal{O}(|\mathcal{I}_m|n)$ . To balance the real-space error,  $|\mathcal{I}_m|$  cannot be chosen too small. For the original Gaussian Ewald split and uniformly random particle locations, the minimal scaling is  $|\mathcal{I}_m| \sim n^{1/2}$ , yielding a total cost of  $\mathcal{O}(n^{3/2})$  [15].

The steps above are summarized in Algorithm 1.

**Algorithm 1** (Direct Fourier-space summation).

*Comment:* The radial mollifier  $\gamma_\sigma$ , with width parameter  $\sigma$  is chosen based on the cut-off  $r_c$ , and the radial Green's function  $G$  are given, such that the mollified kernel satisfies  $\hat{M}(\mathbf{k}) = \hat{G}(|\boldsymbol{\omega}(\mathbf{k})|) \hat{\gamma}_\sigma(|\boldsymbol{\omega}(\mathbf{k})|)$ . Matrix forms are stated in brackets.

*Input:*  $\{\mathbf{x}_j\}_{j=1}^n, \{\rho_j\}_{j=1}^n, L, m$

*Output:*  $\{\phi_j^{\text{far}}\}_{j=1}^n$

1:  $[\hat{\rho} = \mathbf{U} \boldsymbol{\rho}]$  Compute the structure factor:

$$\hat{\rho}(\mathbf{k}) := \sum_{j=1}^n \rho_j e^{\frac{2\pi}{L}i\mathbf{k}\cdot\mathbf{x}_j}, \quad \mathbf{k} \in \mathcal{I}_m.$$

2:  $[\hat{\boldsymbol{\phi}}^{\text{far}} := \mathbf{D} \hat{\rho}]$  Apply diagonal scaling:

$$\hat{\boldsymbol{\phi}}^{\text{far}}(\mathbf{k}) := \begin{cases} \frac{1}{V} \hat{M}(\mathbf{k}) \hat{\rho}(\mathbf{k}), & \mathbf{k} \in \mathcal{I}_m, \\ 0, & \mathbf{k} = \mathbf{0}. \end{cases}$$

3:  $[\boldsymbol{\phi}^{\text{far}} \approx \mathbf{U}^* \hat{\boldsymbol{\phi}}^{\text{far}}]$  Evaluate the adjoint transform:

$$\phi_i^{\text{far}} \approx \sum_{\mathbf{k} \in \mathcal{I}_m} \hat{\boldsymbol{\phi}}^{\text{far}}(\mathbf{k}) e^{-\frac{2\pi}{L}i\mathbf{k}\cdot\mathbf{x}_i}, \quad i = 1, \dots, n.$$

### 3.2 Fast Ewald summation

In fast Ewald methods, the discrete Fourier transforms of parts 1 and 3 in Algorithm 1 are accelerated using FFTs, employing similar components to those used in type 1 and type 2 nonuniform FFTs (NUFFT) [10, 14].

Let  $\tilde{\varphi}$  be a periodized window function whose support is, up to possibly a small numerical tolerance, contained in  $[-\alpha, \alpha]^3$ . Using  $\tilde{\varphi}$ , we spread the  $n$  source strengths  $\{\rho_j\}_{j=1}^n$  onto the uniform grid  $\{h\mathbf{l}\}_{\mathbf{l} \in \mathcal{I}_m}$  with spacing  $h = L/m$ , via

$$a_{\mathbf{l}} := \sum_{j=1}^n \rho_j \tilde{\varphi}(\mathbf{x}_j - h\mathbf{l}), \quad \mathbf{l} \in \mathcal{I}_m. \quad (41)$$

In practice, the sum is evaluated only over the  $P^3$  grid points in the support of  $\tilde{\varphi}$  that yield nonzero contributions, giving a spreading cost of  $\mathcal{O}(P^3 n)$ .

Applying the FFT to  $\{a_{\mathbf{l}}\}_{\mathbf{l} \in \mathcal{I}_m}$  yields

$$\hat{a}_{\mathbf{k}} = \sum_{\mathbf{l} \in \mathcal{I}_m} a_{\mathbf{l}} e^{\frac{2\pi}{L} i \mathbf{k} \cdot (h\mathbf{l})}, \quad \mathbf{k} \in \mathcal{I}_m, \quad (42)$$

which approximates  $\hat{\rho}(\mathbf{k}) \hat{\varphi}(\mathbf{k})$ . To recover an approximation to  $\hat{\rho}(\mathbf{k})$ , it is therefore natural to multiply by  $1/\hat{\varphi}(\mathbf{k})$ , undoing the convolution introduced by the window. Since this multiplication depends only on  $\mathbf{k}$ , it is incorporated into the diagonal scaling step of the algorithm (corresponding to step 2 of Algorithm 1).

Thus, step 1 of Algorithm 1 is approximated using an FFT in  $\mathcal{O}(P^3 n + |\mathcal{I}_m| \log |\mathcal{I}_m|)$ . We emphasize that no oversampling is applied; oversampling would normally be introduced by truncation (or zero-padding) of Fourier modes. In the present setting we assume that the aliasing errors are sufficiently damped by the diagonal scaling; see Remark 12.

Because step 3 of the direct algorithm is the adjoint of step 1, the approximation of step 3 uses the same deconvolution factor,  $1/\hat{\varphi}(\mathbf{k})$ . Thus the total deconvolution factor is  $1/\hat{\varphi}(\mathbf{k})^2$ , which is included in the diagonal scaling. The resulting diagonal scaling step in the fast Ewald method is therefore

$$\hat{b}_{\mathbf{k}} := \frac{1}{V} \frac{\hat{M}(\mathbf{k})}{\hat{\varphi}(\mathbf{k})^2} \hat{a}_{\mathbf{k}}, \quad \mathbf{k} \in \mathcal{I}_m \setminus \{\mathbf{0}\}. \quad (43)$$

Now, the inverse FFT yields  $\{b_{\mathbf{l}}\}_{\mathbf{l} \in \mathcal{I}_m}$ , which are then interpolated back to the particle locations from the uniform grid, yielding the final approximation to the far-field potential:

$$\phi_i^{\text{far}} \approx \sum_{\mathbf{l} \in \mathcal{I}_m} b_{\mathbf{l}} \tilde{\varphi}(\mathbf{x}_i - h\mathbf{l}). \quad (44)$$

Equations (41)–(44) may be written compactly in matrix form as

$$\phi^{\text{far}} \approx \mathbf{S}^T \mathbf{F}^{-1} \mathbf{C} \mathbf{D} \mathbf{F} \mathbf{S} \boldsymbol{\rho}, \quad (45)$$

where  $\mathbf{S}$  denotes spreading,  $\mathbf{F}$  and  $\mathbf{F}^{-1}$  the forward and inverse FFTs,  $\mathbf{D} = V^{-1} \text{diag}(\hat{M}(\mathbf{k}))$ ,  $\mathbf{C} = \text{diag}(\hat{\varphi}(\mathbf{k})^{-2})$ , and  $\mathbf{S}^T$  denotes interpolation.

Thus, the overall cost of evaluating the Fourier-space component is

$$\mathcal{O}(P^3 n + |\mathcal{I}_m| \log |\mathcal{I}_m|), \quad (46)$$

that is, linear in the number of particles plus the FFT cost, with  $P$  the window support size. For typical parameter choices with  $|\mathcal{I}_m| \propto n$ , this yields an overall complexity of  $\mathcal{O}(n \log n)$ .

The steps of the fast Ewald method, as presented above, are summarized in Algorithm 2.

**Algorithm 2** (Fast Fourier-space summation).

*Comment:* The radial mollifier  $\gamma_\sigma$ , with width parameter  $\sigma$  chosen based on the cutoff  $r_c$ , the radial Green's function  $G$  such that  $\hat{M}(\mathbf{k}) = \hat{G}(|\boldsymbol{\omega}(\mathbf{k})|) \hat{\gamma}_\sigma(|\boldsymbol{\omega}(\mathbf{k})|)$ , and the window function  $\varphi$  whose periodization is used for spreading and interpolation, are given. Matrix forms are stated in brackets.

*Input:*  $\{\mathbf{x}_j\}_{j=1}^n$ ,  $\{\rho_j\}_{j=1}^n$ ,  $L$ ,  $m$

*Output:*  $\{\phi_j^{\text{far}}\}_{j=1}^n$

1:  $[\mathbf{a} := \mathbf{S} \boldsymbol{\rho}]$  Spread to the uniform grid of spacing  $h = L/m$ :

$$a_l := \sum_{j=1}^n \rho_j \tilde{\varphi}(\mathbf{x}_j - h\mathbf{l}), \quad \mathbf{l} \in \mathcal{I}_m.$$

2:  $[\hat{\mathbf{a}} = \mathbf{F} \mathbf{a}]$  3D FFT on the grid:

$$\hat{a}_{\mathbf{k}} = \sum_{\mathbf{l} \in \mathcal{I}_m} a_{\mathbf{l}} e^{\frac{2\pi i}{L} \mathbf{k} \cdot (h\mathbf{l})}, \quad \mathbf{k} \in \mathcal{I}_m.$$

3:  $[\hat{\mathbf{b}} := \mathbf{C} \mathbf{D} \hat{\mathbf{a}}]$  Diagonal scaling (omit  $\mathbf{k} = \mathbf{0}$ ):

$$\hat{b}_{\mathbf{k}} := \begin{cases} \frac{1}{V} \frac{\hat{M}(\mathbf{k})}{\hat{\varphi}(\mathbf{k})^2} \hat{a}_{\mathbf{k}}, & \mathbf{k} \in \mathcal{I}_m \setminus \{\mathbf{0}\}, \\ 0, & \mathbf{k} = \mathbf{0}. \end{cases}$$

4:  $[\mathbf{b} = \mathbf{F}^{-1} \hat{\mathbf{b}}]$  Inverse FFT:

$$b_{\mathbf{l}} = \sum_{\mathbf{k} \in \mathcal{I}_m} \hat{b}_{\mathbf{k}} e^{-\frac{2\pi i}{L} \mathbf{k} \cdot (h\mathbf{l})}, \quad \mathbf{l} \in \mathcal{I}_m.$$

5:  $[\phi^{\text{far}} \approx \mathbf{S}^T \mathbf{b}]$  Interpolate to particle locations:

$$\phi_i^{\text{far}} \approx \sum_{\mathbf{l} \in \mathcal{I}_m} b_{\mathbf{l}} \tilde{\varphi}(\mathbf{x}_i - h\mathbf{l}), \quad i = 1, \dots, n.$$

**Remark 5.** Alternative conventions shift window factors differently, giving equivalent schemes with modified diagonal scaling (e.g., SPME [11]).

## 4 Fast Ewald summation for the Laplace kernel using the first PSWF of order zero

In this section, we present how the first PSWF of order zero,  $\psi_0^c$ , can be employed both as a mollifier in the Ewald-split and as a window function for the spreading/interpolation steps of Algorithm 2.

#### 4.1 General Ewald decomposition for numerical mollifiers with support $[-1, 1]$

Let  $\gamma_1$  be an even, nonnegative numerical mollifier with  $\text{supp}(\gamma_1) = [-1, 1]$  and normalization  $\int_{\mathbb{R}} \gamma_1(u) du = 1$ . Define a one-dimensional *split function*  $\Phi: \mathbb{R} \rightarrow \mathbb{R}$  by

$$\Phi(x) := 2 \int_0^x \gamma_1(u) du. \quad (47)$$

Scaling  $\gamma_1$  to a cutoff radius  $r_c > 0$ , define

$$\gamma_{r_c}(x) := \frac{1}{r_c} \gamma_1\left(\frac{x}{r_c}\right), \quad (48)$$

which is also a numerical mollifier with support  $[-r_c, r_c]$ , inheriting the same properties as  $\gamma_1$ .

Now, by Lemma 1, the three-dimensional mollification of the Laplace Green's function is

$$M(\mathbf{x}) = \frac{\Phi_{r_c}(|\mathbf{x}|)}{|\mathbf{x}|}, \quad (49)$$

where

$$\Phi_{r_c}(x) := \Phi(x/r_c) = 2 \int_0^{x/r_c} \gamma_1(v) dv = 2 \int_0^x \gamma_{r_c}(u) du. \quad (50)$$

Its Fourier transform then satisfies

$$\hat{M}(\boldsymbol{\omega}) = \frac{4\pi}{|\boldsymbol{\omega}|^2} \hat{\gamma}_{r_c}(|\boldsymbol{\omega}|). \quad (51)$$

Finally, substituting (49) in the Ewald decomposition  $G = M + R$  the residual kernel becomes

$$R(\mathbf{x}) = \frac{1 - \Phi_{r_c}(|\mathbf{x}|)}{|\mathbf{x}|}. \quad (52)$$

**Remark 6.** Because  $\gamma_1$  is nonnegative and normalized, we have  $0 \leq \Phi_{r_c}(x) \leq 1$  for all  $x \geq 0$ , ensuring that the residual kernel  $R(\mathbf{x})$  is nonnegative.

**Remark 7.** Since the unscaled mollifier  $\gamma_1$  satisfies  $\int_{-1}^1 \gamma_1(u) du = 1$ , we have  $\Phi(1) = 1$ ; hence  $\Phi_{r_c}(x) = 1$  for all  $x \geq r_c$ . In this case, the residual kernel (52) is compactly supported on the ball of radius  $r_c$ , since  $R(\mathbf{x}) = 0$  whenever  $|\mathbf{x}| \geq r_c$ . A construction of a split function of this type was first presented for the PSWF in the DMK framework [17].

#### 4.2 A PSWF mollifier for the Ewald split

Following Section 4.1, we now construct a PSWF mollifier. We start by defining an unscaled mollifier  $\gamma_1^{cs}$ , supported on  $[-1, 1]$ , as

$$\gamma_1^{cs}(x) := \begin{cases} \frac{\psi_0^{cs}(x)}{\hat{\psi}_0^{cs}(0)} = \frac{\psi_0^{cs}(x)}{\lambda_0 \psi_0^{cs}(0)}, & x \in [-1, 1], \\ 0, & x \notin [-1, 1], \end{cases} \quad (53)$$

where  $\psi_0^{c_s}$  denotes the first PSWF with Fourier bandlimit  $c_s > 0$  (the subscript “s” stands for “split”). Here,  $\lambda_0$  is the eigenvalue associated with  $\psi_0^{c_s}$ , and the identity  $\hat{\psi}_0^{c_s}(0) = \lambda_0 \psi_0^{c_s}(0)$  follows from Lemma 2. This normalization ensures that  $\int_{\mathbb{R}} \gamma_1^{c_s}(x) dx = \int_{-1}^1 \gamma_1^{c_s}(x) dx = 1$ . Then, to obtain a mollifier supported on a general radius  $r_c > 0$ , we scale  $\gamma_1^{c_s}$  as

$$\gamma_{r_c}^{c_s}(x) := \frac{1}{r_c} \gamma_1^{c_s}\left(\frac{x}{r_c}\right) = \begin{cases} \frac{\psi_0^{c_s}(x/r_c)}{r_c \lambda_0 \psi_0^{c_s}(0)}, & x \in [-r_c, r_c], \\ 0, & x \notin [-r_c, r_c], \end{cases} \quad (54)$$

which inherits the mollifier properties of  $\gamma_1^{c_s}$ . In contrast to the Gaussian mollifier, whose width parameter  $\sigma$  is free, the PSWF mollifier is compactly supported on  $[-r_c, r_c]$ . Consequently, the effective width parameter coincides with the cutoff radius, that is,  $\sigma = r_c$ .

The Fourier transform of  $\gamma_{r_c}^{c_s}$  admits a closed-form expression within the band  $[-c_s/r_c, c_s/r_c]$ :

$$\hat{\gamma}_{r_c}^{c_s}(\omega) = \hat{\gamma}_1^{c_s}(r_c \omega) = \frac{\psi_0^{c_s}(r_c \omega / c_s)}{\psi_0^{c_s}(0)}, \quad \omega \in \left[-\frac{c_s}{r_c}, \frac{c_s}{r_c}\right]. \quad (55)$$

Outside this interval, the Fourier transform must be evaluated directly from its defining integral,

$$\hat{\gamma}_{r_c}^{c_s}(\omega) = \int_{-r_c}^{r_c} \gamma_{r_c}^{c_s}(x) e^{-i\omega x} dx. \quad (56)$$

We remark that (56) is included only for completeness; the integral representation (56) is never used in practice, since only Fourier modes within the band  $[-c_s/r_c, c_s/r_c]$  are required.

Using  $\gamma_{r_c}^{c_s}$  and (47), we can thus denote a PSWF-based split function that is closely related to the split function introduced in the DMK framework [17] as

$$\Phi_{r_c}^{c_s}(x) := 2 \int_0^x \gamma_{r_c}^{c_s}(u) du = \frac{2}{\lambda_0 \psi_0^{c_s}(0)} \int_0^{x/r_c} \psi_0^{c_s}(v) dv, \quad x \in [0, r_c], \quad (57)$$

where the integral must be evaluated numerically.

Finally, the mollified kernel used in the fast Ewald algorithm (Algorithm 2) can now be written as

$$\hat{M}(\omega) = \frac{4\pi}{|\omega|^2} \hat{\gamma}_{r_c}^{c_s}(|\omega|) = \frac{4\pi}{|\omega|^2} \frac{\psi_0^{c_s}(r_c |\omega| / c_s)}{\psi_0^{c_s}(0)}, \quad |\omega| \leq \frac{c_s}{r_c}, \quad (58)$$

and the residual kernel for the real-space sum is obtained from the split function (57) via (52).

As stated in Remark 7, the residual kernel is compactly supported by construction. Figure 2 shows  $\Phi_{0.5}^{c_s}(x)$  and a cross-section of the corresponding residual kernel for  $r_c = 0.5$  and various values of  $c_s$ , illustrating both the compact support and the dependence on  $c_s$ .

Table 1 summarizes the PSWF-based mollifier alongside the classical Gaussian mollifier derived in Example 1. For a comparison of their spectral decay and support, see also Figure 1.

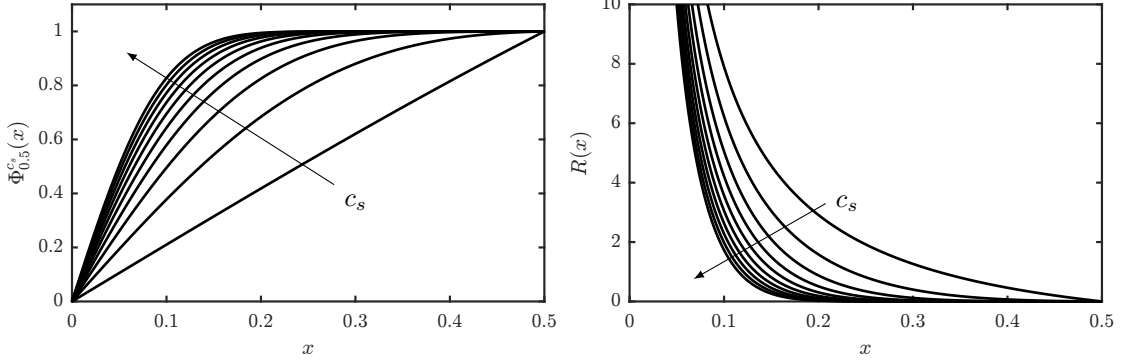


**Figure 2:** Split function  $\Phi_{r_c}^{c_s}(x)$  (left) and residual kernel  $R(x)$  (right) for  $r_c = 0.5$  and  $c_s \in \{1, 6, 11, \dots, 49\}$ . By construction, the split function satisfies  $\Phi_{r_c}^{c_s}(r_c) = 1$ , and the residual kernel is compactly supported on  $[-r_c, r_c]$ .

**Table 1:** Gaussian and PSWF-based mollifiers. The Gaussian mollifier has width parameter  $\sigma$ , while the PSWF mollifier is compactly supported with cutoff  $r_c$  and bandlimit  $c_s$ . The fact that  $\hat{\gamma}_{r_c}^{\text{PSWF}}(\omega)$  does not admit a closed-form expression outside the interval  $[-c_s/r_c, c_s/r_c]$  is unimportant in practice, since this region is never used.

Definition in real space	Fourier transform
$\gamma_\sigma^{\text{Gauss}}(x) = \frac{1}{\sqrt{\pi}\sigma} e^{-x^2/\sigma^2}$	$\hat{\gamma}_\sigma^{\text{Gauss}}(\omega) = e^{-\sigma^2\omega^2/4}$
$\gamma_{r_c}^{\text{PSWF}}(x) = \begin{cases} \frac{\psi_0^{c_s}(x/r_c)}{r_c \lambda_0 \psi_0^{c_s}(0)}, & x \in [-r_c, r_c] \\ 0, & \text{otherwise} \end{cases}$	$\hat{\gamma}_{r_c}^{\text{PSWF}}(\omega) = \begin{cases} \frac{\psi_0^{c_s}(r_c\omega/c_s)}{\psi_0^{c_s}(0)} & \omega \in \left[-\frac{c_s}{r_c}, \frac{c_s}{r_c}\right] \\ \text{no closed form,} & \text{otherwise} \end{cases}$

### 4.3 A PSWF window function

Analogous to the PSWF mollifier, we introduce two parameters for a PSWF window function: a shape (bandlimit) parameter  $c_w > 0$  (with  $w$  denoting ‘‘window’’), which controls spectral concentration and decay, and a width parameter  $\alpha > 0$ , which determines the window half-width.

We define a one-dimensional, unscaled window function by

$$\varphi_1^{c_w}(x) := \frac{\psi_0^{c_w}(x)}{\psi_0^{c_w}(0)}, \quad x \in \mathbb{R}. \quad (59)$$

By Lemma 2, its Fourier transform for  $\omega \in [-c_w, c_w]$  is given by

$$\hat{\varphi}_1^{c_w}(\omega) = \lambda_0 \frac{\psi_0^{c_w}(\omega/c_w)}{\psi_0^{c_w}(0)}. \quad (60)$$

A three-dimensional window function  $\varphi^{c_w} : \mathbb{R}^3 \rightarrow \mathbb{R}$  is constructed by rescaling  $\varphi_1^{c_w}$  and forming a tensor product of the resulting one-dimensional windows. This choice provides a natural extension from one to three dimensions while preserving the optimal concentration properties of the underlying one-dimensional PSWF, and it allows the Fourier transform to factorize into a product of one-dimensional transforms, thereby

simplifying both the theoretical analysis and the numerical implementation:

$$\varphi^{c_w}(\mathbf{x}) := \prod_{i=1}^3 \varphi_1^{c_w}(x_i/\alpha) = \prod_{i=1}^3 \frac{\psi_0^{c_w}(x_i/\alpha)}{\psi_0^{c_w}(0)}. \quad (61)$$

The Fourier transform of  $\varphi^{c_w}$  has per-coordinate bandlimit  $|\omega_i| \leq c_w/\alpha$  and is given by

$$\hat{\varphi}^{c_w}(\boldsymbol{\omega}) = \prod_{i=1}^3 \alpha \hat{\varphi}_1^{c_w}(\alpha\omega_i) = \left( \frac{\alpha \lambda_0}{\psi_0^{c_w}(0)} \right)^3 \prod_{i=1}^3 \psi_0^{c_w} \left( \frac{\alpha\omega_i}{c_w} \right). \quad (62)$$

Finally, recalling Section 2.4, the truncated window is defined as

$$\varphi_t^{c_w}(\mathbf{x}) := \begin{cases} \varphi^{c_w}(\mathbf{x}), & \mathbf{x} \in [-\alpha, \alpha]^3, \\ 0, & \mathbf{x} \notin [-\alpha, \alpha]^3, \end{cases} \quad (63)$$

with periodization given by  $\tilde{\varphi}_t^{c_w}(\mathbf{x}) = \sum_{\mathbf{r} \in \mathbb{Z}^3} \varphi_t^{c_w}(\mathbf{x} + L\mathbf{r})$ .

The truncated window  $\varphi_t^{c_w}(\mathbf{x})$  with Fourier transform given by  $\hat{\varphi}^{c_w}(\boldsymbol{\omega})$  in  $[-c_w/\alpha, c_w/\alpha]^3$  is what we will refer to as the PSWF window function; see Table 2.

**Remark 8.** Due to the tensor-product structure, the gradient of  $\varphi^{c_w}$  is

$$\frac{\partial \varphi^{c_w}}{\partial x_j}(\mathbf{x}) = \frac{1}{\alpha \psi_0^{c_w}(0)^3} \frac{d\psi_0^{c_w}}{ds} \left( \frac{x_j}{\alpha} \right) \prod_{\substack{i=1 \\ i \neq j}}^3 \psi_0^{c_w} \left( \frac{x_i}{\alpha} \right), \quad j = 1, 2, 3, \quad (64)$$

where the factor  $1/\alpha$  arises from the chain rule. The derivative  $d\psi_0^{c_w}/ds$  is obtained using the same algorithm as the  $\psi_0^{c_w}$  function; see Appendix B.

Thus, for force computations (e.g.  $\mathbf{F}_i = \rho_i \nabla \phi_i$ ),  $\nabla \phi_i$  can be obtained by replacing the last interpolation step (step 5) in Algorithm 2 with

$$\nabla \phi_i^{far} = \sum_{\mathbf{l} \in \mathcal{I}_m} b_{\mathbf{l}} \nabla \tilde{\varphi}^{c_w}(\mathbf{x}_i - h\mathbf{l}). \quad (65)$$

**Remark 9.** To accelerate window evaluation, the 1D domain may be partitioned into  $w$  intervals, each approximated by a centered polynomial of degree  $p = w + 3$ , precomputed via a Vandermonde system and then evaluated efficiently using Horner's rule and SIMD vectorization [5]. This has been shown to yield a 2–3 times speed-up for spreading and interpolation in 1D for the Kaiser–Bessel function [28].

#### 4.3.1 Comparison of the PSWF window with Gaussian and B-spline windows

Table 2 summarizes the PSWF, Gaussian, and B-spline windows. The Gaussian window is presented here in its non-truncated (free-space) form. In practice, however, the window is truncated in real space, but rather than defining the Gaussian window explicitly as a truncated function, most implementations continue to use the free-space expressions for both the window and its Fourier transform [20, 28]. This practice introduces truncation errors in the spreading and interpolation steps for the Gaussian window—errors that do not arise for B-spline or PSWF windows, which are compactly supported by construction.

**Table 2:** Gaussian, B-spline, and PSWF windows in one dimension. In practice, three-dimensional tensor-product windows  $\varphi(\mathbf{x}) = \prod_{i=1}^3 \varphi(x_i)$  are used. Here  $c_g > 0$  denotes the Gaussian shape parameter,  $\alpha$  the window half-width, and  $P$  the B-spline order (which coincides with the support size). For the Gaussian window, the commonly used free-space form is listed.

Definition in real space	Fourier transform
$\varphi^{\text{Gauss}}(x) = e^{-c_g(x/\alpha)^2}$	$\hat{\varphi}^{\text{Gauss}}(\omega) = \alpha \sqrt{\frac{\pi}{c_g}} e^{-\omega^2 \alpha^2 / (4c_g)}$
$\varphi^{\text{B-spline}}(x) = B_P(x/h)$ where $B_1(x) := \begin{cases} 1, & x \in [-\frac{1}{2}, \frac{1}{2}] \\ 0, & \text{otherwise} \end{cases}$ $B_{P+1}(x) := (B_P * B_1)(x)$	$\hat{\varphi}^{\text{B-spline}}(\omega) = h \hat{B}_P(h\omega)$ where $\hat{B}_P(\omega) := \left( \frac{\sin(\omega/2)}{\omega/2} \right)^P$
$\varphi^{\text{PSWF}}(x) = \begin{cases} \frac{\psi_0^{c_w}(x/\alpha)}{\psi_0^{c_w}(0)}, & x \in [-\alpha, \alpha] \\ 0, & \text{otherwise} \end{cases}$	$\hat{\varphi}^{\text{PSWF}}(\omega) = \begin{cases} \alpha \lambda_0 \frac{\psi_0^{c_w}(\alpha\omega/c_w)}{\psi_0^{c_w}(0)}, & \omega \in \left[ -\frac{c_w}{\alpha}, \frac{c_w}{\alpha} \right] \\ \text{no closed form,} & \text{otherwise} \end{cases}$

B-splines have support width  $P$ , that equals the spline order, and have Fourier transform  $\hat{\varphi}(\omega) = h \hat{B}_P(h\omega)$ , where  $h$  denotes the grid spacing and  $\hat{B}_P(\omega) = (\sin(\omega/2)/(\omega/2))^P$ . Consequently, their spectral decay is algebraic. For a fixed real-space width  $\alpha$ , B-splines therefore require either a finer grid or a higher order  $P$  to match the accuracy of the PSWF window; increasing  $P$  enlarges the support and increases the cost of spreading and interpolation. The widely used SPME method [11]—implemented, for example, in GROMACS [34]—employs non-centered cardinal B-splines for spreading and interpolation and deconvolves their spectrum through a modified diagonal scaling (see Remark 5). However, the underlying algebraic spectral decay remains unchanged.

## 5 Theoretical error analysis for the PSWF split and window functions

In this section, we present a rigorous theoretical analysis of the error sources arising in fast Ewald summation using PSWF-based functions. We derive absolute  $L^2$  error estimates associated with both the PSWF mollifier and the PSWF window function introduced in Section 4, establishing exponential error decay and providing sharp bounds. For the purpose of parameter selection—where fully rigorous bounds are unnecessarily detailed—we also derive simplified, closed-form error models that are well suited for practical use.

The squared RMS (root-mean-square) error is measured in the volume-normalized  $L^2$  norm,

$$\frac{1}{V} \|f_{\text{ref}} - f\|_{L^2(\Omega)}^2 = \frac{1}{V} \int_{\Omega} |f_{\text{ref}}(\mathbf{x}) - f(\mathbf{x})|^2 d\mathbf{x} \approx \frac{1}{n} \sum_{i=1}^n |f_{\text{ref}}(\mathbf{x}_i) - f(\mathbf{x}_i)|^2, \quad (66)$$

where the approximation is justified by the law of large numbers when the particle locations  $\{\mathbf{x}_i\}_{i=1}^n$  are chosen independently and uniformly from  $\Omega$ . In this setting, the discrete average converges to the continuous integral as  $n \rightarrow \infty$ .

Let  $\phi_t^{\text{far}}$  denote the truncated far-field sum  $\phi^{\text{far}}$ , and let  $\phi_{t,h}^{\text{far}}$  denote an approximation of  $\phi_t^{\text{far}}$  computed using the fast Ewald algorithm (Algorithm 2). In fast Ewald summation, two principal sources of error arise: (i) truncation of Fourier modes in the Fourier-transformed mollified kernel—referred to as *split errors*—quantified by  $\frac{1}{\sqrt{V}} \|\phi^{\text{far}} - \phi_t^{\text{far}}\|_{L^2(\Omega)}$ , and (ii) *approximation errors* arising in the spreading and interpolation steps, quantified by  $\frac{1}{\sqrt{V}} \|\phi_t^{\text{far}} - \phi_{t,h}^{\text{far}}\|_{L^2(\Omega)}$ .

When the residual kernel is not compactly supported, additional truncation errors arise in the real-space sum. However, for PSWF-based mollifiers, the residual kernel  $R$  is compactly supported, and real-space truncation errors are therefore eliminated. This further simplifies the analysis.

By the triangle inequality, the total error can be bounded as

$$\frac{1}{\sqrt{V}} \|\phi^{\text{far}} - \phi_{t,h}^{\text{far}}\|_{L^2(\Omega)} \leq \frac{1}{\sqrt{V}} \|\phi^{\text{far}} - \phi_t^{\text{far}}\|_{L^2(\Omega)} + \frac{1}{\sqrt{V}} \|\phi_t^{\text{far}} - \phi_{t,h}^{\text{far}}\|_{L^2(\Omega)}. \quad (67)$$

Consequently, contributions (i) and (ii) may be analyzed separately.

## 5.1 Ewald-split truncation errors

Suppose that the errors of the DFT steps in Algorithm 2 (steps 1–2 and 4–5) are negligible. Then the total error depends on the choice of mollifier used in the split and Algorithm 2 turns into Algorithm 1. In this subsection we analyze these split-errors.

We start with a small lemma that relates to the structure factor  $\hat{\rho}(\mathbf{k})$  and the distribution of points. It is important since Ewald summation is most efficient when the points are close to uniformly random. The lemma provides a uniform bound on the Fourier coefficients of  $\rho$  at frequencies above the cutoff  $K_{\max}$ . In particular, it shows that the energy contained in any high-frequency mode  $\hat{\rho}(\mathbf{k})$  cannot exceed a constant multiple of the total  $\ell_2$ -energy of  $\rho$ .

**Lemma 3.** *For all  $\mathbf{k} \in \mathbb{Z}^3$ , the Fourier coefficients of the particle density satisfy*

$$|\hat{\rho}(\mathbf{k})|^2 \leq C_\rho \|\rho\|_2^2, \quad (68)$$

where  $0 < C_\rho \leq n$ .

*Proof.* By the definition of the discrete Fourier transform, we have

$$\hat{\rho}(\mathbf{k}) = \sum_{j=1}^n \rho_j e^{\frac{2\pi}{L} i \mathbf{k} \cdot \mathbf{x}_j}. \quad (69)$$

Applying the Cauchy–Schwarz inequality and using that each exponential factor has modulus one, we obtain

$$|\hat{\rho}(\mathbf{k})|^2 \leq \left( \sum_{j=1}^n |\rho_j|^2 \right) \left( \sum_{j=1}^n |e^{\frac{2\pi}{L} i \mathbf{k} \cdot \mathbf{x}_j}|^2 \right) = n \|\rho\|_2^2. \quad (70)$$

Thus

$$C_\rho := \max_{\mathbf{k} \in \mathbb{Z}^3} \frac{|\hat{\rho}(\mathbf{k})|^2}{\|\rho\|_2^2} \leq n, \quad (71)$$

which proves the result.  $\square$

**Remark 10.** The constant  $C_\rho$  reflects the degree of cancellation among the oscillatory exponential terms. In the worst case (highly clustered particles), one may have  $C_\rho$  as large as  $n$ . However, for well-distributed configurations (e.g., approximately uniform particle distributions), the exponential vectors corresponding to distinct wavenumbers are nearly orthogonal, leading to substantial cancellations. In such cases, it is reasonable to assume that  $C_\rho \approx 1$ .

We are now ready to state the following lemma, which provides an error estimate for the far-field direct sum for a general mollifier  $\gamma_\sigma$ .

**Lemma 4.** Let  $\phi_t^{\text{far}}$  denote the Fourier-space far-field sum truncated to modes  $|k_i| \leq K_{\max}$  for  $i = 1, 2, 3$ . Then the squared RMS-error of the truncation satisfies

$$\frac{1}{V} \|\phi^{\text{far}} - \phi_t^{\text{far}}\|_{L^2(\Omega)}^2 \leq \frac{8C_\rho \|\rho\|_2^2}{V} \int_{\omega_*}^{\infty} |\hat{\gamma}_\sigma(\omega)|^2 \frac{1}{\omega^2} d\omega, \quad (72)$$

where  $V = L^3$ ,  $C_\rho$  is the constant from Lemma 3, and  $\omega_* := \max\{\omega_{\max} - \frac{\sqrt{3}\pi}{L}, 0\}$ .

*Proof.* By Parseval's theorem,

$$\frac{1}{V} \|\phi^{\text{far}} - \phi_t^{\text{far}}\|_{L^2(\Omega)}^2 = \frac{1}{V^2} \sum_{|\mathbf{k}| > K_{\max}} |\hat{\rho}(\mathbf{k})|^2 |\hat{M}(\mathbf{k})|^2. \quad (73)$$

Using Lemma 3,

$$\frac{1}{V} \|\phi^{\text{far}} - \phi_t^{\text{far}}\|_{L^2(\Omega)}^2 \leq \frac{C_\rho \|\rho\|_2^2}{V^2} \sum_{|\mathbf{k}| > K_{\max}} |\hat{M}(\mathbf{k})|^2. \quad (74)$$

Since  $|\hat{M}(\mathbf{k})|^2$  is radial and nonincreasing in  $|\mathbf{k}|$ , the lattice-to-continuum estimate of Lemma 6 (Appendix C.3) yields the bound

$$\sum_{|\mathbf{k}| > K_{\max}} |\hat{M}(\mathbf{k})|^2 \leq \left(\frac{L}{2\pi}\right)^3 \int_{|\boldsymbol{\omega}| > \omega_*} |\hat{M}(\boldsymbol{\omega})|^2 d\boldsymbol{\omega}, \quad \omega_* = \max\{\omega_{\max} - \frac{\sqrt{3}\pi}{2L}, 0\}. \quad (75)$$

Passing to spherical coordinates,

$$\int_{|\boldsymbol{\omega}| > \omega_*} |\hat{M}(\boldsymbol{\omega})|^2 d\boldsymbol{\omega} = 4\pi \int_{\omega_*}^{\infty} |\hat{M}(\omega)|^2 \omega^2 d\omega. \quad (76)$$

With  $\hat{M}(\omega) = \frac{4\pi}{\omega^2} \hat{\gamma}_\sigma(\omega)$ ,

$$\int_{\omega_*}^{\infty} |\hat{M}(\omega)|^2 \omega^2 d\omega = 16\pi^2 \int_{\omega_*}^{\infty} \frac{|\hat{\gamma}_\sigma(\omega)|^2}{\omega^2} d\omega. \quad (77)$$

Collecting constants from Parseval's theorem, the radial integral, and the lattice-to-continuum bound, and using  $V = L^3$ , we obtain the prefactor 8:

$$\frac{1}{V^2} \sum_{|\mathbf{k}| > K_{\max}} |\hat{M}(\mathbf{k})|^2 \leq \frac{8}{V} \int_{\omega_*}^{\infty} \frac{|\hat{\gamma}_\sigma(\omega)|^2}{\omega^2} d\omega. \quad (78)$$

Multiplying by  $C_\rho \|\rho\|_2^2$  completes the proof.  $\square$

Even though the PSWF function  $\psi_0^{c_s}$  is implicit in nature, Theorem 1 allows us to evaluate its  $L^2$  norm exactly for  $\omega_{\max} = c_s/r_c$ . The following proposition, which follows from Lemma 4, estimates the PSWF split-errors.

**Proposition 1.** *Let  $\phi_t^{\text{far}}$  denote the Fourier-space far-field sum truncated to modes  $|k_i| \leq K_{\max}$  for  $i = 1, 2, 3$ , and let the PSWF mollifier be given by (54)–(55). Suppose that  $\omega_{\max} = c_s/r_c$  and  $\omega_* = \omega_{\max} - \frac{\sqrt{3}\pi}{L}$  so that  $\omega_* \in (0, \omega_{\max})$ , and define*

$$C_* := 1 + \left( \frac{\omega_{\max}}{\omega_*} \right)^2 \frac{c_s \lambda_0^2}{2\pi - c_s \lambda_0^2}. \quad (79)$$

Then the squared RMS-error satisfies

$$\frac{1}{V} \|\phi^{\text{far}} - \phi_t^{\text{far}}\|_{L^2(\Omega)}^2 \leq \frac{4 C_\rho C_* r_c \|\rho\|_2^2}{V c_s^2 \psi_0^{c_s}(0)^2} \left( \frac{2\pi}{\lambda_0^2} - c_s \right), \quad (80)$$

where  $V = L^3$  and  $0 < C_\rho \leq n$  is the constant from Lemma 3.

*Proof.* By Lemma 4,

$$\frac{1}{V} \|\phi^{\text{far}} - \phi_t^{\text{far}}\|_{L^2(\Omega)}^2 \leq \frac{8 C_\rho}{V} \|\rho\|_2^2 \int_{\omega_*}^{\infty} \frac{|\hat{\gamma}_{r_c}^{c_s}(\omega)|^2}{\omega^2} d\omega. \quad (81)$$

Splitting the integral at  $\omega_{\max}$  and using that  $\omega \mapsto \omega^{-2}$  is decreasing,

$$\int_{\omega_*}^{\infty} \frac{|\hat{\gamma}_{r_c}^{c_s}(\omega)|^2}{\omega^2} d\omega \leq \frac{1}{\omega_*^2} \int_{\omega_*}^{\omega_{\max}} |\hat{\gamma}_{r_c}^{c_s}(\omega)|^2 d\omega + \frac{1}{\omega_{\max}^2} \int_{\omega_{\max}}^{\infty} |\hat{\gamma}_{r_c}^{c_s}(\omega)|^2 d\omega. \quad (82)$$

Since  $\int_{\omega_*}^{\omega_{\max}} \leq \int_0^{\omega_{\max}}$ , we relate the in-band and tail energies using the PSWF scaling

$$\hat{\gamma}_{r_c}^{c_s}(\omega) = \frac{1}{\lambda_0 \psi_0^{c_s}(0)} \hat{\psi}_0^{c_s}(u) \Big|_{u=r_c\omega}. \quad (83)$$

Hence,

$$\frac{\int_0^{\omega_{\max}} |\hat{\gamma}_{r_c}^{c_s}(\omega)|^2 d\omega}{\int_{\omega_{\max}}^{\infty} |\hat{\gamma}_{r_c}^{c_s}(\omega)|^2 d\omega} = \frac{\int_0^{c_s} |\hat{\psi}_0^{c_s}(u)|^2 du}{\int_{c_s}^{\infty} |\hat{\psi}_0^{c_s}(u)|^2 du} = \frac{c_s \lambda_0^2}{2\pi - c_s \lambda_0^2}, \quad (84)$$

where we used Theorem 1 and evenness. Therefore,

$$\int_{\omega_*}^{\infty} \frac{|\hat{\gamma}_{r_c}^{c_s}(\omega)|^2}{\omega^2} d\omega \leq \left( \left( \frac{\omega_{\max}}{\omega_*} \right)^2 \frac{c_s \lambda_0^2}{2\pi - c_s \lambda_0^2} + 1 \right) \frac{1}{\omega_{\max}^2} \int_{\omega_{\max}}^{\infty} |\hat{\gamma}_{r_c}^{c_s}(\omega)|^2 d\omega. \quad (85)$$

With the change of variables  $u = r_c\omega$  and  $\omega_{\max} = c_s/r_c$ , and substituting  $\hat{\gamma}_{r_c}^{c_s}(\omega) = \psi_0^{c_s}(r_c\omega/c_s)/\psi_0^{c_s}(0)$ , the tail integral becomes

$$\begin{aligned} \int_{\omega_{\max}}^{\infty} |\hat{\gamma}_{r_c}^{c_s}(\omega)|^2 d\omega &= \frac{1}{\lambda_0^2 \psi_0^{c_s}(0)^2 r_c} \int_{c_s}^{\infty} |\hat{\psi}_0^{c_s}(u)|^2 du \\ &= \frac{1}{\lambda_0^2 \psi_0^{c_s}(0)^2 r_c} \frac{1}{2} (2\pi - c_s \lambda_0^2), \end{aligned} \quad (86)$$

again using Theorem 1 and evenness.

Combining these identities yields

$$\int_{\omega_*}^{\infty} \frac{|\hat{\gamma}_{r_c}^{c_s}(\omega)|^2}{\omega^2} d\omega \leq \frac{C_* r_c}{2 c_s^2 \psi_0^{c_s}(0)^2} \left( \frac{2\pi}{\lambda_0^2} - c_s \right). \quad (87)$$

Multiplying by  $\frac{8C_\rho}{V} \|\boldsymbol{\rho}\|_2^2$  gives the claimed bound.  $\square$

**Remark 11.** *The leading PSWF eigenvalue depends on the bandlimit,  $\lambda_0 = \lambda_0(c_s)$ . It is known (see, e.g., [24, p. 42]) that, as  $c_s \rightarrow \infty$ ,*

$$\frac{2\pi}{\lambda_0^2} \sim c_s. \quad (88)$$

Hence

$$\frac{2\pi}{c_s \lambda_0^2} - 1 = \frac{1}{c_s} \left( \frac{2\pi}{\lambda_0^2} \right) - 1 \rightarrow 0 \quad \text{as } c_s \rightarrow \infty. \quad (89)$$

This convergence is exponentially fast (see Appendix A and [9, 29]). However, numerically this expression is the difference of two nearly equal terms, which leads to catastrophic cancellation in double precision. As a result,  $2\pi/(c_s \lambda_0^2) - 1$  cannot be evaluated reliably for  $c_s \gtrsim 17$ . Using the known asymptotic behavior of  $\lambda_0$ , this quantity can instead be evaluated via a stable and accurate approximation (see Figure 9).

### 5.1.1 A closed form approximation for the split truncation error

Although the bound in Proposition 1 is rigorous, it cannot be evaluated reliably for large  $c_s$  due to subtractive cancellation (see Remark 11). Moreover, its asymptotic decay is not immediately useful for parameter selection. For practical purposes, we therefore introduce an exponential approximation, fitted to numerical data, that captures the decay of the error with high accuracy over the parameter ranges of interest.

Assuming the particle positions are well distributed (i.e., without significant clustering), we may set  $C_\rho \approx 1$  as in Remark 10. Furthermore, the prefactor  $C_*$  in Proposition 1 accounts for the contribution from the interval  $[\omega_*, \omega_{\max}]$ . In practical settings, where the truncation parameter  $K_{\max}$  is sufficiently large (so that  $\omega_* \approx \omega_{\max}$ ), this factor satisfies  $C_* \approx 1$  and can therefore be neglected. Remark 11 together with the curve-fit in Table 5 (Appendix A) shows that, for  $c_s \gtrsim 10$ , the expression

$$\frac{2}{c_s \psi_0^{c_s}(0)} \sqrt{\frac{2\pi}{\lambda_0^2} - c_s} \quad (90)$$

is well approximated (up to a maximal relative error of  $\approx 0.2\%$ ) by an exponential (see Equation (143) in Appendix A). This motivates the following closed form model

$$\frac{1}{\sqrt{V}} \|\phi^{\text{far}} - \phi_t^{\text{far}}\|_{L^2(\Omega)} \approx \frac{1}{\sqrt{V}} \|\boldsymbol{\rho}\|_2 \sqrt{r_c} A_s c_s^{-1/2} e^{-c_s}, \quad A_s = 6.91. \quad (91)$$

Finally, we stress that the assumption  $C_\rho \approx 1$  is essential: for strongly clustered particle configurations, the error may increase by up to a factor of  $\sqrt{n}$ .

## 5.2 Aliasing errors due to window function approximations

Recall that, in fast Ewald summation, the discrete Fourier transform steps are approximated by convolution with a window function (spreading and interpolation), followed by application of the FFT. These components are closely related to those used in nonuniform FFTs (NUFFTs). Window functions may either be truncated or compactly supported by construction, and the errors introduced by these approximations contribute to the total error together with the split error analyzed in Section 5.1.

In the NUFFT literature, one-dimensional error estimates for various window functions have been derived in [4, 6, 26, 32]. A key parameter in these analyses is the oversampling factor, which controls the magnitude of aliasing errors. Fast Ewald methods, however, are typically implemented without oversampling [20, 28], and we adopt that convention here. Moreover, fast Ewald summation is inherently a three-dimensional problem.

The sources of error arising from the NUFFT components are analogous to those in fast Ewald summation. In practice, all window functions are truncated. As discussed in Section 4.3.1 for the Gaussian window, the use of the untruncated Fourier transform introduces additional errors in the spreading and interpolation steps. These are commonly referred to as *truncation errors*. A second source of error arises from *aliasing*, which is caused by discrete sampling of the window function. Sampling induces a periodization in Fourier space via the Poisson summation formula, leading to overlapping frequency contributions [25, p. 124].

The PSWF window function is compactly supported by definition and admits an exact Fourier representation for all  $\mathbf{k} \in \mathcal{I}_m$ . Consequently, window truncation errors are absent, and only aliasing errors need to be analyzed. To avoid ambiguity in the more general results, we retain the subscript  $t$  and write  $\tilde{\varphi}_t$  (like we define the PSWF window in Section 4.3) to emphasize that the window is both periodic and compactly supported.

From the NUFFT literature, it is known that aliasing errors in the spreading and interpolation steps admit similar estimates [32]. Therefore, we restrict our attention to aliasing errors arising from the interpolation step.

Recall that the interpolation step in Algorithm 2 approximates a truncated function on the form

$$f(\mathbf{x}) = \sum_{\mathbf{k} \in \mathcal{I}_m} \hat{f}_{\mathbf{k}} e^{-\frac{2\pi}{L} i \mathbf{k} \cdot \mathbf{x}}. \quad (92)$$

It is approximated using translates (convolution) of a window function,

$$f(\mathbf{x}) \approx f_h(\mathbf{x}) := \sum_{l \in \mathcal{I}_m} g_l \tilde{\varphi}_t(\mathbf{x} - h\mathbf{l}) = \sum_{\mathbf{k} \in \mathbb{Z}^3} \hat{g}_{\mathbf{k}} c_{\mathbf{k}}(\tilde{\varphi}_t) e^{-\frac{2\pi}{L} i \mathbf{k} \cdot \mathbf{x}}. \quad (93)$$

Here  $\hat{g}_{\mathbf{k}}$  denotes the discrete Fourier coefficients of the grid values  $\{g_l\}_{l \in \mathcal{I}_m}$  on the  $\mathbf{m}$ -grid, extended periodically in frequency, so that

$$\hat{g}_{\mathbf{k}+mr} = \hat{g}_{\mathbf{k}}, \quad \mathbf{k} \in \mathcal{I}_m, \quad \mathbf{r} \in \mathbb{Z}^3. \quad (94)$$

We choose

$$\hat{g}_{\mathbf{k}} := \frac{\hat{f}_{\mathbf{k}}}{c_{\mathbf{k}}(\tilde{\varphi}_t)}, \quad \mathbf{k} \in \mathcal{I}_m, \quad (95)$$

with the convention that  $c_{\mathbf{k}}(\tilde{\varphi}_t) \neq 0$  for  $\mathbf{k} \in \mathcal{I}_m$ . This choice can be interpreted as a deconvolution by  $c_{\mathbf{k}}(\tilde{\varphi}_t)$  and is the one employed in Algorithm 2. It has been shown to be accurate even in the presence of aliasing [21]. This leads to the following result.

**Lemma 5** (Aliasing error relation). *Suppose that  $f$  and  $f_h$  are given by (92) and (93), with  $\hat{g}_{\mathbf{k}}$  defined by (95). Assume further that  $c_{\mathbf{k}}(\tilde{\varphi}_t) \neq 0$  for all  $\mathbf{k} \in \mathcal{I}_m$ . Then*

$$\frac{1}{V} \|f - f_h\|_{L^2(\Omega)}^2 = \sum_{\mathbf{k} \in \mathcal{I}_m} |\hat{f}_{\mathbf{k}}|^2 \sum_{\mathbf{r} \in \mathbb{Z}^3 \setminus \{\mathbf{0}\}} \frac{|c_{\mathbf{k}+m\mathbf{r}}(\tilde{\varphi}_t)|^2}{|c_{\mathbf{k}}(\tilde{\varphi}_t)|^2}. \quad (96)$$

*Proof.* We have

$$\begin{aligned} f_h(\mathbf{x}) &= \sum_{\mathbf{k} \in \mathbb{Z}^3} \hat{g}_{\mathbf{k}} c_{\mathbf{k}}(\tilde{\varphi}_t) e^{-\frac{2\pi}{L} i \mathbf{k} \cdot \mathbf{x}} \\ &= \sum_{\mathbf{k} \in \mathcal{I}_m} \hat{g}_{\mathbf{k}} c_{\mathbf{k}}(\tilde{\varphi}_t) e^{-\frac{2\pi}{L} i \mathbf{k} \cdot \mathbf{x}} + \sum_{\mathbf{k} \in \mathcal{I}_m} \sum_{\mathbf{r} \in \mathbb{Z}^3 \setminus \{\mathbf{0}\}} \hat{g}_{\mathbf{k}+m\mathbf{r}} c_{\mathbf{k}+m\mathbf{r}}(\tilde{\varphi}_t) e^{-\frac{2\pi}{L} i (\mathbf{k}+m\mathbf{r}) \cdot \mathbf{x}}. \end{aligned} \quad (97)$$

Subtracting (97) from (92) and using the periodicity  $\hat{g}_{\mathbf{k}+m\mathbf{r}} = \hat{g}_{\mathbf{k}}$  yields

$$\begin{aligned} f(\mathbf{x}) - f_h(\mathbf{x}) &= \sum_{\mathbf{k} \in \mathcal{I}_m} (\hat{f}_{\mathbf{k}} - \hat{g}_{\mathbf{k}} c_{\mathbf{k}}(\tilde{\varphi}_t)) e^{-\frac{2\pi}{L} i \mathbf{k} \cdot \mathbf{x}} \\ &\quad - \sum_{\mathbf{k} \in \mathcal{I}_m} \sum_{\mathbf{r} \in \mathbb{Z}^3 \setminus \{\mathbf{0}\}} \hat{g}_{\mathbf{k}} c_{\mathbf{k}+m\mathbf{r}}(\tilde{\varphi}_t) e^{-\frac{2\pi}{L} i (\mathbf{k}+m\mathbf{r}) \cdot \mathbf{x}}. \end{aligned} \quad (98)$$

The two sums are supported on disjoint frequency sets and are therefore orthogonal in  $L^2(\Omega)$ . Parseval's theorem gives

$$\|f - f_h\|_{L^2(\Omega)}^2 = V \sum_{\mathbf{k} \in \mathcal{I}_m} |\hat{f}_{\mathbf{k}} - \hat{g}_{\mathbf{k}} c_{\mathbf{k}}(\tilde{\varphi}_t)|^2 + V \sum_{\mathbf{k} \in \mathcal{I}_m} \sum_{\mathbf{r} \in \mathbb{Z}^3 \setminus \{\mathbf{0}\}} |\hat{g}_{\mathbf{k}}|^2 |c_{\mathbf{k}+m\mathbf{r}}(\tilde{\varphi}_t)|^2. \quad (99)$$

Using (95), the first sum vanishes and  $|\hat{g}_{\mathbf{k}}|^2 = |\hat{f}_{\mathbf{k}}|^2 / |c_{\mathbf{k}}(\tilde{\varphi}_t)|^2$ . Substitution yields (96).  $\square$

**Remark 12** (Oversampling). *Since  $c_{\mathbf{k}}(\tilde{\varphi}_t)$  is even and monotonically decreasing in  $|\mathbf{k}|$  for  $|\mathbf{k}| > 0$ , there exist indices  $\mathbf{k} \in \mathcal{I}_m$  and  $\mathbf{r} \in \mathbb{Z}^3 \setminus \{\mathbf{0}\}$  such that  $|\mathbf{k} + m\mathbf{r}| \leq |\mathbf{k}|$ , implying*

$$\frac{c_{\mathbf{k}+m\mathbf{r}}^2(\tilde{\varphi}_t)}{c_{\mathbf{k}}^2(\tilde{\varphi}_t)} \geq 1. \quad (100)$$

*Hence, in the absence of oversampling, aliasing errors are not uniformly suppressed by the window function alone.*

*Nevertheless, the diagonal scaling in fast Ewald methods—contained in the  $|\hat{f}_{\mathbf{k}}|^2$  factor—damps this effect.*

Using Lemma 5 we can now estimate the aliasing errors of Algorithm 2 for the PSWF mollifier and the PSWF window function.

**Proposition 2** (Aliasing error in interpolation). *Let  $\phi_t^{\text{far}}$  be the truncated Fourier-space far-field potential produced by Algorithm 1, using the PSWF mollifier  $\gamma_{r_c}^{cs}$ , with the Fourier series representation*

$$\phi_t^{\text{far}}(\mathbf{x}) = \frac{1}{V} \sum_{\mathbf{k} \in \mathcal{I}_m \setminus \{\mathbf{0}\}} \hat{M}(\mathbf{k}) \hat{\rho}(\mathbf{k}) e^{-\frac{2\pi i}{L} \mathbf{k} \cdot \mathbf{x}}. \quad (101)$$

Let  $\phi_{t,h}^{\text{far}}$  denote its approximation obtained by the interpolation step of Algorithm 2, using the PSWF window  $\tilde{\varphi}_t^{c_w}$ .

For the purpose of the analysis, we employ the deconvolution choice

$$\hat{g}_{\mathbf{k}} := \frac{1}{V} \frac{\hat{M}(\mathbf{k}) \hat{\rho}(\mathbf{k})}{c_{\mathbf{k}}(\tilde{\varphi}_t^{c_w})}, \quad \mathbf{k} \in \mathcal{I}_m, \quad (102)$$

where  $c_{\mathbf{k}}(\tilde{\varphi}_t^{c_w})$  denotes the Fourier series coefficient of the periodized window.

Then the interpolation error satisfies

$$\frac{1}{V} \|\phi_t^{\text{far}} - \phi_{t,h}^{\text{far}}\|_{L^2(\Omega)}^2 \leq \frac{C_{\rho} L \|\boldsymbol{\rho}\|_2^2}{V \pi^2 \psi_0^{c_s}(0)^2} \sum_{\mathbf{k} \in \mathcal{I}_m \setminus \{\mathbf{0}\}} \frac{\psi_0^{c_s}(\frac{2}{m}|\mathbf{k}|)^2 \sum_{\mathbf{r} \in \mathbb{Z}^3 \setminus \{\mathbf{0}\}} \prod_{i=1}^3 \psi_0^{c_w}\left(\frac{2}{m}(k_i + m r_i)\right)^2}{|\mathbf{k}|^4 \prod_{i=1}^3 \psi_0^{c_w}\left(\frac{2}{m}k_i\right)^2}, \quad (103)$$

where  $0 < C_{\rho} \leq n$  is the constant from Lemma 3.

*Proof.* By Lemma 5, applied to  $\phi_{t,h}^{\text{far}}$ , and using Lemma 3 together with  $\hat{M}(\mathbf{k}) = \hat{G}(\mathbf{k}) \hat{\gamma}_{r_c}^{c_s}(|\mathbf{k}|)$ , we obtain

$$\begin{aligned} \frac{1}{V} \|\phi_t^{\text{far}} - \phi_{t,h}^{\text{far}}\|_{L^2(\Omega)}^2 &= \frac{1}{V^2} \sum_{\mathbf{k} \in \mathcal{I}_m \setminus \{\mathbf{0}\}} |\hat{M}(\mathbf{k}) \hat{\rho}(\mathbf{k})|^2 \sum_{\mathbf{r} \in \mathbb{Z}^3 \setminus \{\mathbf{0}\}} \frac{c_{\mathbf{k}+m\mathbf{r}}^2(\tilde{\varphi}_t^{c_w})}{c_{\mathbf{k}}^2(\tilde{\varphi}_t^{c_w})} \\ &\leq \frac{C_{\rho}}{V^2} \|\boldsymbol{\rho}\|_2^2 \sum_{\mathbf{k} \in \mathcal{I}_m \setminus \{\mathbf{0}\}} |\hat{G}(\mathbf{k}) \hat{\gamma}_{r_c}^{c_s}(|\mathbf{k}|)|^2 \sum_{\mathbf{r} \in \mathbb{Z}^3 \setminus \{\mathbf{0}\}} \frac{c_{\mathbf{k}+m\mathbf{r}}^2(\tilde{\varphi}_t^{c_w})}{c_{\mathbf{k}}^2(\tilde{\varphi}_t^{c_w})}. \end{aligned} \quad (104)$$

By (19),  $c_{\mathbf{k}}(\tilde{\varphi}_t^{c_w}) = \frac{1}{V} \hat{\varphi}_t^{c_w}(\mathbf{k})$ . Using  $\omega_i/\omega_{\max} = 2k_i/m$ , this ratio can be written as

$$\frac{c_{\mathbf{k}+m\mathbf{r}}^2(\tilde{\varphi}_t^{c_w})}{c_{\mathbf{k}}^2(\tilde{\varphi}_t^{c_w})} = \frac{\prod_{i=1}^3 \psi_0^{c_w}\left(\frac{2}{m}(k_i + m r_i)\right)^2}{\prod_{i=1}^3 \psi_0^{c_w}\left(\frac{2}{m}k_i\right)^2}, \quad (105)$$

where the normalization constants in  $\tilde{\varphi}_t^{c_w}$  cancel. With  $\omega = 2\pi|\mathbf{k}|/L$  and  $r_c = c_s L/(\pi m)$  we have

$$\frac{r_c \omega}{c_s} = \frac{2}{m} |\mathbf{k}|, \quad (106)$$

so the PSWF argument simplifies as claimed. Substituting  $\hat{G}(\mathbf{k}) = L^2/(\pi|\mathbf{k}|^2)$  and the explicit representation of  $\hat{\gamma}_{r_c}^{c_s}$  yields

$$\frac{1}{V} \|\phi_t^{\text{far}} - \phi_{t,h}^{\text{far}}\|_{L^2(\Omega)}^2 \leq \frac{C_{\rho} L^4 \|\boldsymbol{\rho}\|_2^2}{V^2 \pi^2 \psi_0^{c_s}(0)^2} \sum_{\mathbf{k} \in \mathcal{I}_m \setminus \{\mathbf{0}\}} \left| \frac{\psi_0^{c_s}(\frac{2}{m}|\mathbf{k}|)}{|\mathbf{k}|^2} \right|^2 \sum_{\mathbf{r} \in \mathbb{Z}^3 \setminus \{\mathbf{0}\}} \frac{\prod_{i=1}^3 \psi_0^{c_w}\left(\frac{2}{m}(k_i + m r_i)\right)^2}{\prod_{i=1}^3 \psi_0^{c_w}\left(\frac{2}{m}k_i\right)^2}. \quad (107)$$

Substituting  $V = L^3$  then gives the desired estimate (103).  $\square$

### 5.2.1 A closed-form approximation for the aliasing error

In (103), the aliasing sum is dominated by the first nonzero terms with  $|\mathbf{r}| = 1$ , since the PSWF window decays rapidly with  $|\mathbf{r}|$ . These six contributions—corresponding to one shift in each coordinate direction in three dimensions—provide the leading-order contribution to the aliasing error. We therefore approximate (103) by retaining only these terms, yielding

$$\frac{1}{V} \|\phi_t^{\text{far}} - \phi_{t,h}^{\text{far}}\|_{L^2(\Omega)}^2 \approx \frac{C_\rho L \|\boldsymbol{\rho}\|_2^2}{V \pi^2 \psi_0^{c_s}(0)^2} \sum_{\mathbf{k} \in \mathcal{I}_m \setminus \{\mathbf{0}\}} \frac{\psi_0^{c_s}\left(\frac{2}{m}|\mathbf{k}|\right)^2 \sum_{|\mathbf{r}|=1} \prod_{i=1}^3 \psi_0^{c_w}\left(\frac{2}{m}(k_i + mr_i)\right)^2}{|\mathbf{k}|^4 \prod_{i=1}^3 \psi_0^{c_w}\left(\frac{2}{m}k_i\right)^2}. \quad (108)$$

Since  $|\mathbf{k}| \geq |k_i|$  and  $\psi_0^c$  is even and nonincreasing on  $[0, \infty)$ , we have

$$\psi_0^{c_s}\left(\frac{2}{m}|\mathbf{k}|\right) \leq \psi_0^{c_s}\left(\frac{2}{m}|k_i|\right), \quad i \in \{1, 2, 3\}. \quad (109)$$

Equality holds for axis-aligned modes of the form  $\mathbf{k} = s k \mathbf{e}_j$ , where  $s \in \{\pm 1\}$ ,  $j \in \{1, 2, 3\}$ , and  $k \in \{1, \dots, K_{\max}\}$  with  $K_{\max} = \lfloor m/2 \rfloor$ . For such modes,

$$\frac{\psi_0^{c_s}\left(\frac{2}{m}|\mathbf{k}|\right)^2}{\prod_{i=1}^3 \psi_0^{c_w}\left(\frac{2}{m}k_i\right)^2} = \frac{\psi_0^{c_s}\left(\frac{2}{m}k\right)^2}{\psi_0^{c_w}\left(\frac{2}{m}k\right)^2 \psi_0^{c_w}(0)^4} \approx \frac{1}{\psi_0^{c_w}(0)^4}, \quad (110)$$

where the approximation uses  $c_s \approx c_w$  with  $c_s < c_w$  (see Section 7).

Next, for  $k_i \in \mathcal{I}_m$  and  $r_i \in \{\pm 1\}$ ,

$$\left| \frac{2}{m}(k_i + mr_i) \right| \in [1, 3], \quad \left| \frac{2}{m}k_i \right| \in (0, 1], \quad (111)$$

and by evenness and monotonicity of  $\psi_0^{c_w}$ ,

$$\prod_{i=1}^3 \psi_0^{c_w}\left(\frac{2}{m}(k_i + mr_i)\right)^2 \leq \psi_0^{c_w}(1)^2 \psi_0^{c_w}(0)^4. \quad (112)$$

Equality occurs (for even  $m$ ) in the extremal axis-aligned case where  $\left| \frac{2}{m}(k_j + mr_j) \right| = 1$ , i.e.,  $|k_j| = K_{\max}$  and  $r_j = -\text{sgn}(k_j)$ .

Collecting terms, we obtain

$$\sum_{\mathbf{k} \in \mathcal{I}_m \setminus \{\mathbf{0}\}} \frac{\sum_{|\mathbf{r}|=1} \prod_{i=1}^3 \psi_0^{c_w}\left(\frac{2}{m}(k_i + mr_i)\right)^2}{|\mathbf{k}|^4 \prod_{i=1}^3 \psi_0^{c_w}\left(\frac{2}{m}k_i\right)^2} \approx 6 \psi_0^{c_w}(1)^2 \sum_{k=1}^{K_{\max}} \frac{1}{k^4} < \psi_0^{c_w}(1)^2 \frac{\pi^4}{15}, \quad (113)$$

where the factor 6 accounts for three coordinate axes and two signs, and  $\sum_{k \geq 1} k^{-4} = \pi^4/90$ .

Substituting (113) into (108) yields the dimensionless prefactor  $C_\rho \pi^2/15 \approx 0.66 C_\rho$ , which is of order unity and independent of  $m$ ,  $L$ , and  $c_w$ . We thus arrive at the approximation

$$\frac{1}{\sqrt{V}} \|\phi_t^{\text{far}} - \phi_{t,h}^{\text{far}}\|_{L^2(\Omega)} \approx \frac{1}{\sqrt{V}} \frac{\pi}{\sqrt{15}} \sqrt{C_\rho L} \|\boldsymbol{\rho}\|_2 \frac{\psi_0^{c_w}(1)}{\psi_0^{c_w}(0)}. \quad (114)$$

Assuming well-distributed particles so that  $C_\rho \approx 1$ , and approximating  $\psi_0^{c_w}(1)/\psi_0^{c_w}(0)$  accurately (up to a maximal relative error of  $\approx 1.5\%$ ) by curve-fitting (see Table 5 in Appendix A), yields the final closed form model for the aliasing error

$$\frac{1}{\sqrt{V}} \|\phi_t^{\text{far}} - \phi_{t,h}^{\text{far}}\|_{L^2(\Omega)} \approx \frac{1}{\sqrt{V}} A_w \sqrt{L} \|\rho\|_2 c_w^{1/2} e^{-c_w}, \quad A_w \approx 2.78. \quad (115)$$

Numerical experiments show that both the split-error model (91) and the aliasing-error model (115) closely match the observed absolute RMS errors produced by Algorithm 2; see Figure 4.

## 6 Parameter selection

This section presents practical guidelines for selecting the PSWF mollifier and window parameters to achieve a prescribed tolerance  $\varepsilon$ . The results rely on the error models of Section 5. Unless otherwise noted, we assume neutral, well-distributed particle configurations so that  $C_\rho \approx 1$  (cf. Remark 10), no oversampling, and parameters  $c_s, c_w$  within the fitted ranges of Table 5.

For simplicity, we assume that  $m$  is even throughout this section; in the odd case, one can replace  $m/2$  by  $\lfloor m/2 \rfloor$ .

### 6.1 Notes about nondimensionalization and the cuboid setting

The Ewald parameters depend only on ratios of characteristic lengths, and are therefore invariant under uniform rescaling of the problem. This allows them to be selected using a normalized cutoff, for example  $r_c/L$  in the cubic case.

For the periodic cubic domain  $[0, L)^3$ , we can define nondimensional coordinates  $\mathbf{x}^* := \mathbf{x}/L \in [0, 1)^3$ . In these variables, the computational domain becomes the unit cube. Periodic functions may then be expanded in the Fourier basis  $e^{2\pi i \mathbf{k} \cdot \mathbf{x}^*}$ , for  $\mathbf{k} \in \mathbb{Z}^3$ , which corresponds in physical coordinates to wavevectors  $2\pi(\mathbf{k}/L)$ . In this setting, it is natural to introduce the dimensionless cutoff

$$r_c^* := \frac{r_c}{L}, \quad 0 < r_c^* < 1, \quad (116)$$

and to express all algorithmic parameters—such as  $c_s, c_w$ , and the grid size  $P$ —in terms of  $r_c^*$  and the target tolerance  $\varepsilon$ . Once these parameters are fixed, physical quantities are recovered by rescaling lengths by  $L$ .

The free-space Laplace kernel satisfies  $G(\mathbf{x}) = 1/|\mathbf{x}|$ , and under the isotropic scaling  $\mathbf{x} = L\mathbf{x}^*$  one has  $G(\mathbf{x}) = \frac{1}{L} G(\mathbf{x}^*)$ . Accordingly, the periodic potential may be written as

$$\phi(\mathbf{x}_i) = \frac{1}{L} \phi^*(\mathbf{x}_i^*), \quad \phi^*(\mathbf{x}_i^*) = \sum_{\mathbf{r} \in \mathbb{Z}^3} \sum_{j=1}^n G(|\mathbf{x}_i^* - \mathbf{x}_j^* + \mathbf{r}|) \rho_j. \quad (117)$$

Hence, we can always solve on the unit cube, using a dimensionless  $r_c$  that accounts for  $L \neq 1$ , and in the end scale the potential with  $L$ .

**Remark 13** (Cuboid domains). *As noted in the introduction, the method extends naturally to cuboid domains. Let  $\Omega = \prod_{j=1}^3 [0, L_j)$  and choose the FFT grid so that each direction uses  $m_i$  points with a common grid spacing  $h$  satisfying  $h = L_i/m_i$ ,  $i = 1, 2, 3$ .*

With  $m_i$  even, this corresponds to representing  $m_i/2$  Fourier modes per direction, and the largest resolved wave number is  $\omega_{\max} = \pi m_i / L_i = \pi / h$ . After introducing the componentwise scaled coordinates  $\mathbf{x}^* = \mathbf{x} / L_{\min}$ , where  $L_{\min} := \min \mathbf{L}$ , the nondimensionalization proceeds as in the cubic case. In particular, the radial cutoff becomes  $r_c^* = r_c / L_{\min}$ , in analogy with (116). The algorithm itself is unchanged, and the Ewald parameters depend only on the relative cutoff size, not on the absolute domain dimensions or its aspect ratio.

## 6.2 PSWF split parameters

Two parameters control the Ewald split: the shape parameter  $c_s$  and the cutoff  $r_c$ . The cutoff balances the real- and Fourier-space costs, while  $c_s$  determines the number of Fourier modes. They are related by (see (55))

$$\frac{c_s}{r_c} = \omega_{\max} = \frac{2\pi}{L} K_{\max} = \frac{\pi m}{L}. \quad (118)$$

Thus, given  $c_s$  and  $r_c$ , it is reasonable to set  $m$  to

$$m \approx \left\lceil \frac{L c_s}{\pi r_c} \right\rceil. \quad (119)$$

### 6.2.1 Choosing $c_s$

A simple choice for  $c_s$  is to use the asymptotic estimate  $c_s \sim \log(1/\varepsilon)$  [17, 19]. However, this choice tends to overestimate  $c_s$  for the small to moderate values of  $c_s$  (see Figure 4). Using the fitted model (91), we instead recommend choosing  $c_s$  as

$$c_s \approx \frac{1}{2} W\left(2 \left(B_s/\varepsilon\right)^2\right), \quad B_s := \frac{1}{\sqrt{V}} A_s \|\boldsymbol{\rho}\|_2 \sqrt{r_c}. \quad (120)$$

where  $W$  is the Lambert  $W$  function.

### 6.2.2 Choosing $r_c$

In molecular simulations (e.g., GROMACS [34]), the real-space cutoff  $r_c$  is often set empirically from physical interaction ranges (e.g., 9 Å) rather than chosen optimally for computational efficiency. In the present formulation, we suggest that  $r_c$  should be treated as a tunable parameter balancing the real- and Fourier-space costs; note that  $r_c$  is linked to  $m$  through (119). The optimal value of  $r_c$  depends on several factors, such as hardware, software, particle number  $n$ , and particle distribution, and is best found empirically by measuring the total runtime for a range of  $r_c$  values.

## 6.3 Window parameters

If both the PSWF mollifier and the PSWF window are used, their scaled bandlimits should match, yielding

$$\frac{c_s}{r_c} = \frac{c_w}{\alpha}. \quad (121)$$

Hence, given  $c_s$ ,  $r_c$ , and  $c_w$ , the window half-width should satisfy

$$\alpha = \frac{r_c c_w}{c_s}. \quad (122)$$

Moreover, the window half-width is  $\alpha = PL/(2m)$ , which gives

$$P = \left\lceil \frac{2m\alpha}{L} \right\rceil. \quad (123)$$

This relation makes the parameters match closely, also after applying rounding to  $m$ ; see Remark 14 below. However, using (118) (assuming  $m$  is even) together with  $\alpha = Ph/2$ , we also obtain the simple relation between  $c_w$  and  $P$ ,

$$c_w = \frac{\pi}{2}P, \quad (124)$$

showing clearly that  $P$  is proportional to  $c_w$ .

### 6.3.1 Choosing $c_w$

To choose  $c_w$ , we assume that the split and window errors are equal. Balancing (115) and (91) we get

$$\sqrt{L} A_w c_w^{1/2} e^{-c_w} = \sqrt{r_c} A_s c_s^{-1/2} e^{-c_s}. \quad (125)$$

We then solve (125) for  $c_w$  using the Lambert  $W$  function and obtain

$$c_w \approx -\frac{1}{2}W\left(-2B_w^2 \frac{e^{-2c_s}}{c_s}\right), \quad B_w := \frac{A_s}{A_w} \sqrt{\frac{r_c}{L}}. \quad (126)$$

## 6.4 Parameter selection procedure

A typical parameter selection procedure for the PSWF/PSWF method is presented in Algorithm 3 below.

**Algorithm 3** (Parameter selection procedure for the PSWF/PSWF method).

*Comment:* The number of particles  $n$ , the source strengths  $\rho$ , and the box size  $L$  are given.

*Input:* Tolerance  $\varepsilon$  and cutoff radius  $r_c$ .

*Output:*  $c_s, c_w, m, P, \alpha$ .

- 1: Solve  $c_s = \frac{1}{2}W(2(B_s/\varepsilon)^2)$  for  $c_s$ , where  $B_s := \frac{1}{\sqrt{V}}A_s\|\rho\|_2\sqrt{r_c}$ .
- 2: Solve  $c_w = -\frac{1}{2}W\left(-2B_w^2 \frac{e^{-2c_s}}{c_s}\right)$  for  $c_w$ , where  $B_w := \frac{A_s}{A_w} \sqrt{\frac{r_c}{L}}$ .
- 3: Set  $\alpha = r_c c_w / c_s$ .
- 4: Set  $m = \lceil L c_s / (\pi r_c) \rceil$ .
- 5: Set  $P = \lceil 2\alpha m / L \rceil$ .

**Remark 14.** Algorithm 3 yields an absolute RMS error that closely matches the prescribed tolerance  $\varepsilon$  (see Figure 7 in Section 7). This agreement arises because the rounding of  $P$  and  $m$  via (123) and (119) is of comparable relative magnitude and therefore effectively balanced. An alternative approach to selecting  $P$  is to use (124) and set  $P = \lceil (2/\pi)c_w \rceil$ . However, depending on the extent of the rounding applied to  $P$ , this choice may result in an effective value of  $c_w$  that is too small, and consequently in a computed error that deviates more from  $\varepsilon$ .

## 7 Numerical results

The algorithms were implemented in MATLAB, with PSWFs computed to high accuracy using `Chebfun` and its built-in `pswf` routine [33]. For general-purpose use, the efficient algorithm described in Appendix B and in [23] can be implemented in any high-performance programming language to evaluate PSWF functions. Timing results for a parallel implementation in GROMACS are reported in [19].

### 7.1 Experimental setup

Unless otherwise stated, we consider systems of  $n = 100$  particles uniformly distributed in  $[0, 1]^3$ , generated using MATLAB's `rand` function. The particle charges  $\rho_j$  are sampled independently from a standard normal distribution (mean 0, variance 1) and subsequently shifted to enforce charge neutrality,  $\sum_j \rho_j = 0$ . The choice  $n = 100$  is sufficient to capture the relevant convergence trends; larger systems exhibit the same slopes and offsets; see e.g. Figure 7. Unless otherwise stated, we set the cutoff radius to  $r_c = 0.1$  and the domain size to  $L = 1$ , which provides reasonable Fourier-space resolution for testing purposes.

We compute the approximate far-field potential values  $\phi^{\text{far}} = (\phi_j^{\text{far}})_{j=1}^n$  using Algorithm 2 and compare them with a reference solution  $\phi_{\text{ref}}^{\text{far}} = (\phi_{\text{ref},j}^{\text{far}})_{j=1}^n$ , obtained by direct Ewald summation (Algorithm 1). In the reference calculation, we employ a sufficiently large number of Fourier modes so that the residual error is at machine precision. The Fourier-transformed mollifier is evaluated at all available wavenumbers (also outside the bandlimit) without additional truncation.

Gaussian window functions are defined as in Table 2. For the B-spline results, we employ cardinal B-splines of order  $P$  together with the standard SPME diagonal scaling [20, Appendix A].

Errors are reported either as relative  $\ell_2$  errors,

$$\frac{\|\phi_{\text{ref}}^{\text{far}} - \phi^{\text{far}}\|_2}{\|\phi_{\text{ref}}^{\text{far}}\|_2}, \quad (127)$$

or as absolute root-mean-square (RMS) errors,

$$\frac{1}{\sqrt{n}} \|\phi_{\text{ref}}^{\text{far}} - \phi^{\text{far}}\|_2, \quad (128)$$

where  $\|\mathbf{a}\|_2 = \sqrt{\sum_{j=1}^n |a_j|^2}$  denotes the standard  $\ell_2$  vector norm. Absolute RMS errors are used when comparing numerical results to the theoretical error models in Section 5, which are formulated in terms of absolute errors. Relative  $\ell_2$  errors are used when comparing different mollifier and window-function configurations, particularly when the relative error magnitude is important for the analysis.

### 7.2 Direct Ewald sum: PSWF vs. Gaussian split

To isolate the effect of the mollifier, we compare the PSWF and Gaussian splits in the direct summation of the far-field potential (Algorithm 1), thereby eliminating approximation errors associated with FFT-based acceleration. For this test, the shape parameters are expected to satisfy

$$c_s \approx (r_c/\sigma)^2 \approx \log(1/\varepsilon), \quad (129)$$

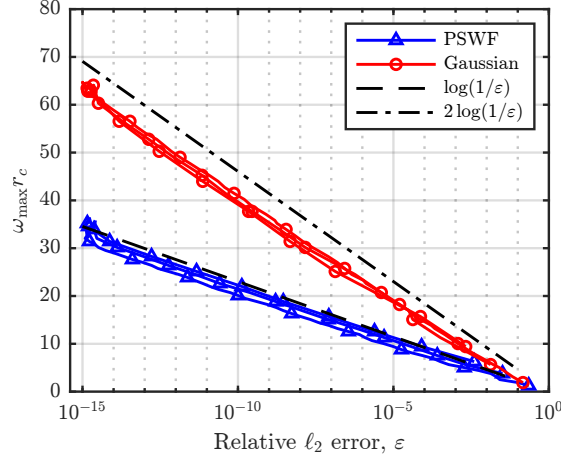


**Figure 3:** Resolution requirements for direct Ewald summation using PSWF and Gaussian splits. Relative  $\ell_2$  errors are shown for cutoff radii  $r_c \in \{0.1, 0.3, 0.5\}$  with  $L = 1$  and  $n = 100$ . Dashed lines indicate reference slopes  $\log(1/\varepsilon)$  (PSWF) and  $2\log(1/\varepsilon)$  (Gaussian). Expressing the resolution as  $\omega_{\max}r_c$  causes the results to collapse and confirms the expected scaling with respect to  $r_c$ . For practically relevant tolerances, the PSWF split requires approximately half as many Fourier modes per dimension, corresponding to an eightfold reduction in three dimensions.

so that  $\psi_0^{c_s}(1)/\psi_0^{c_s}(0) \approx \varepsilon$  for the PSWF split and  $e^{-(r_c/\sigma)^2} \approx \varepsilon$  for the Gaussian split, where  $\varepsilon$  denotes the target relative error for the far-field sum.

For the PSWF split, the optimal number of Fourier modes  $m$  per dimension is directly proportional to the bandlimit  $c_s$  through the relation  $c_s = \omega_{\max}r_c$ , where  $\omega_{\max} = \pi m/L$ . In the Gaussian case, (129) provides a reasonable choice to choose  $\sigma$ . We recall that in the PSWF setting there are no truncation errors in the real-space sum (see Section 4.2), and the split error is therefore entirely determined by the error of the far-field sum. In contrast, for the Gaussian split, the choice of  $\sigma$  must be based on the truncation error of the real-space sum, and (129) sets  $\sigma$  accordingly.

For each  $\sigma$ , the error decreases with increasing  $m$ . To measure the resolution requirements for a given tolerance  $\varepsilon$ , we therefore compute the relative  $\ell_2$  error for increasing values of  $m$  until the measured error falls below  $\varepsilon$ , at which point the corresponding value of  $\omega_{\max} = \pi m/L$  is recorded. The results are shown, together with the errors computed using  $c_s = r_c \omega_{\max}$  for the PSWF split, in Figure 3.

Theoretically, by substituting  $c_s = r_c \omega_{\max}^{\text{PSWF}}$  into  $c_s \approx \log(1/\varepsilon)$ , and  $\sigma^2 \approx r_c^2/\log(1/\varepsilon)$  into the Fourier representation of the Gaussian mollifier,  $e^{-\sigma^2 \omega^2/4} = \varepsilon$  evaluated at  $\omega_{\max}^{\text{Gauss}}$ , one obtains the asymptotic relations

$$\omega_{\max}^{\text{PSWF}} \sim \frac{\log(1/\varepsilon)}{r_c}, \quad \omega_{\max}^{\text{Gauss}} \sim \frac{2\log(1/\varepsilon)}{r_c}. \quad (130)$$

Hence, for a given target tolerance,  $\omega_{\max}^{\text{Gauss}} \approx 2\omega_{\max}^{\text{PSWF}}$ . Figure 3 confirms that the empirical error curves follow these predicted asymptotic trends, implying that the PSWF split requires approximately eight times fewer Fourier modes than the Gaussian split in three dimensions. The figure also indicates that the dependence of the relative error on the cutoff radius  $r_c$  is weak.

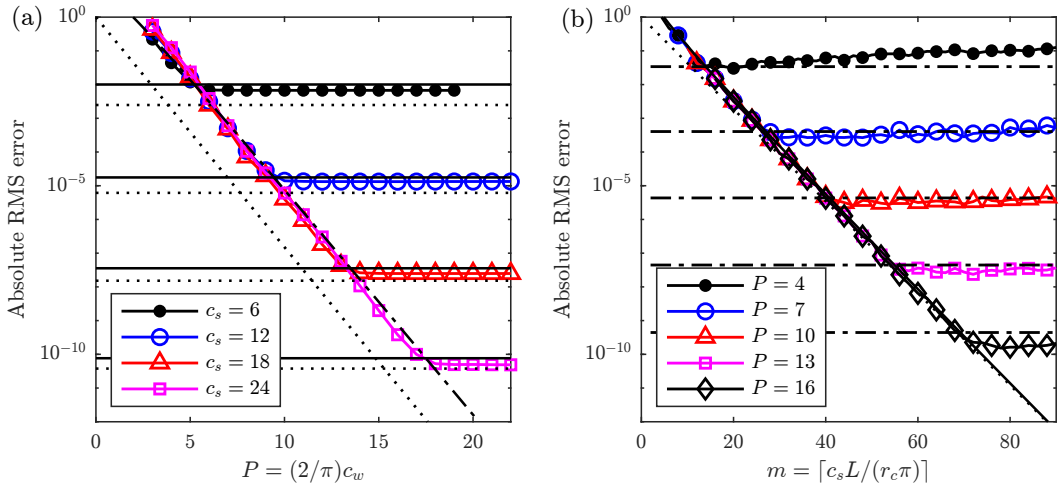


**Figure 4:** Absolute RMS errors for fast Ewald summation (Algorithm 2) using the PSWF split and PSWF window ( $L = 1$ ,  $r_c = 0.1$ ,  $n = 100$ ). Curves with symbols show numerical results, while black curves without symbols show theoretical error models. Dotted lines indicate the simple asymptotic exponential model  $e^{-\{c_s, c_w\}}$ ; solid lines correspond to the split-error model  $\varepsilon = \frac{1}{\sqrt{V}} \sqrt{r_c} \|\rho\|_2 A_s c_s^{-1/2} e^{-c_s}$  (91); and dash-dotted lines correspond to the aliasing-error model  $\varepsilon = \frac{1}{\sqrt{V}} \sqrt{L} \|\rho\|_2 A_w c_w^{1/2} e^{-c_w}$  (115). (a) Absolute RMS error vs. window support  $P = (2/\pi)c_w$  for fixed  $c_s$ . (b) Absolute RMS error vs. number of Fourier modes  $m$  (equivalently  $c_s$ ) for fixed  $P$ .

### 7.3 Fast Ewald with PSWF split and PSWF window

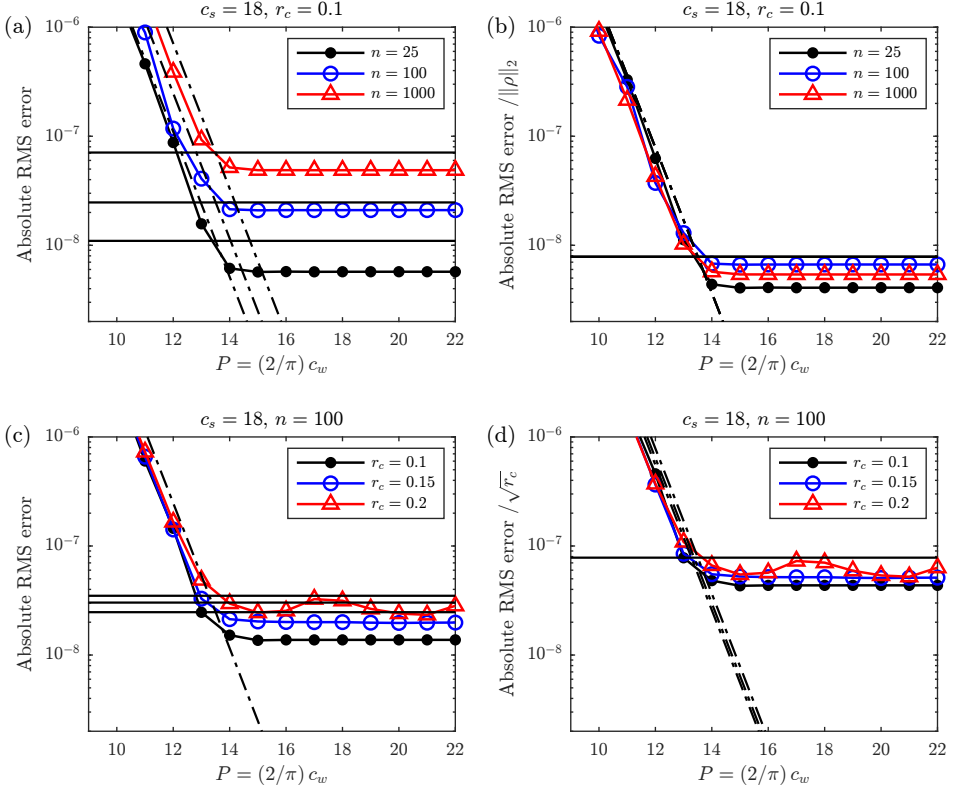
When both the Ewald mollifier and the window function are based on PSWFs, the overall accuracy depends on two shape parameters:  $c_s$ , which controls the Ewald split, and  $c_w$ , which governs the window function. Proposition 2 shows that the aliasing error decays rapidly as  $c_w$  increases, while Proposition 1 characterizes the truncation error associated with  $c_s$ . The total error may be viewed as approximately additive in these two contributions (see (67)) and is dominated by the larger of the two.

Figure 4(a) shows that, for fixed  $c_s$ , the computed absolute RMS error decreases as  $\mathcal{O}(e^{-c_w})$  until it reaches a plateau determined by the split error, which scales as  $\mathcal{O}(e^{-c_s})$ . The fact that this plateau appears perfectly horizontal on a semilogarithmic scale is consistent with the exponential decay.

Conversely, Figure 4(b) demonstrates that increasing  $c_s$ —or, equivalently, increasing the number of Fourier modes  $m$ —reduces the split error until the total error saturates at a level  $\mathcal{O}(e^{-c_w})$ , where  $c_w = (\pi/2)P$ . This saturation level is determined by the aliasing errors introduced by the windowing (spreading and interpolation) steps.

We observe that the error curves and plateaus in Figure 4 are well approximated by the error models (91) and (115). The theoretical predictions accurately capture both the slopes and the plateau levels, with only a slight overestimation of the error. This indicates that the chosen parameter values yield computed errors that are close to—and effectively bounded by—the prescribed tolerance  $\varepsilon$ .

Figures 5(a)–(b) confirm that the absolute RMS error grows nearly linearly with  $\|\rho\|_2$ . After rescaling by  $\|\rho\|_2$ , the error curves nearly collapse, in agreement with the linearity of the potential. That this collapse is not exact is also expected: since the particle configurations are not perfectly uniformly random, the prefactor  $C_\rho$  in Lemma 3 (see also Remark 10) need not be exactly one. In the worst-case scenario



**Figure 5:** Dependence of the absolute RMS error on the system size  $n$  and the cutoff radius  $r_c$  for fast Ewald summation with PSWF split and PSWF mollifier. (a) Window support vs. absolute RMS error for varying  $n$ . (b) Same data as in (a), rescaled by  $\|\rho\|_2$ . (c) Window support vs. absolute RMS error for varying  $r_c$ . (d) Same data as in (c), rescaled by  $\sqrt{r_c}$ . Curves with symbols show numerical results, while black curves without symbols indicate theoretical error models: solid and dash-dotted lines correspond to the split-error model  $\varepsilon = \frac{1}{\sqrt{V}} \sqrt{r_c} \|\rho\|_2 A_s c_s^{-1/2} e^{-c_s}$  (91), and the aliasing-error model  $\varepsilon = \frac{1}{\sqrt{V}} \sqrt{L} \|\rho\|_2 A_w c_w^{1/2} e^{-c_w}$  (115) respectively.

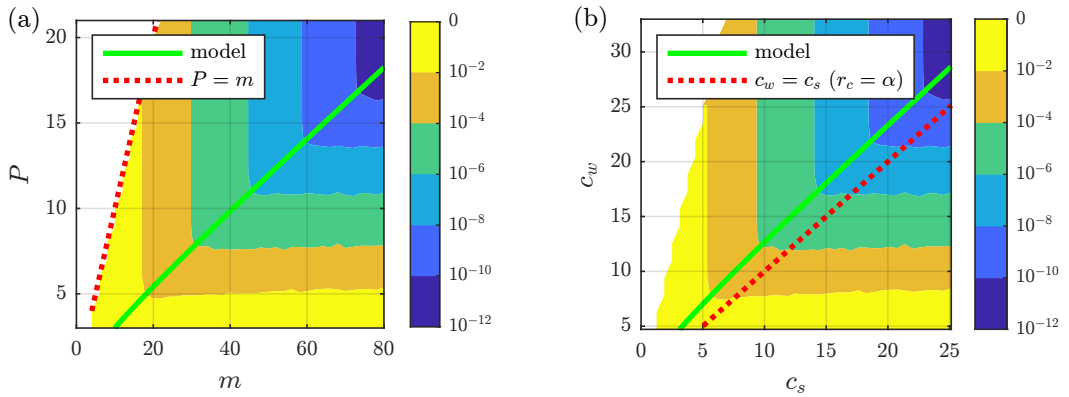


**Figure 6:** Contour plots of the absolute RMS error ( $L = 1$ ,  $r_c = 0.1$ ,  $n = 100$ ). In (a), error in  $(m, P)$  space. In (b), error in  $(c_s, c_w)$  space. The two parameter spaces are related linearly by  $c_s = (\pi r_c / L) m$  and  $c_w = (\pi/2) P$ . The green curve in each panel shows the theoretical optimal relation (125); the computed minimizers  $(m, P)$  (or equivalently  $(c_s, c_w)$ ) for each error level align closely with this curve. For reference, the curve  $P = m$  is also shown, indicating a simple but non-optimal parameter choice, as well as the curve  $c_w = c_s$ , corresponding to the case  $r_c = \alpha$ , which overestimates  $c_s$  for a given error level.

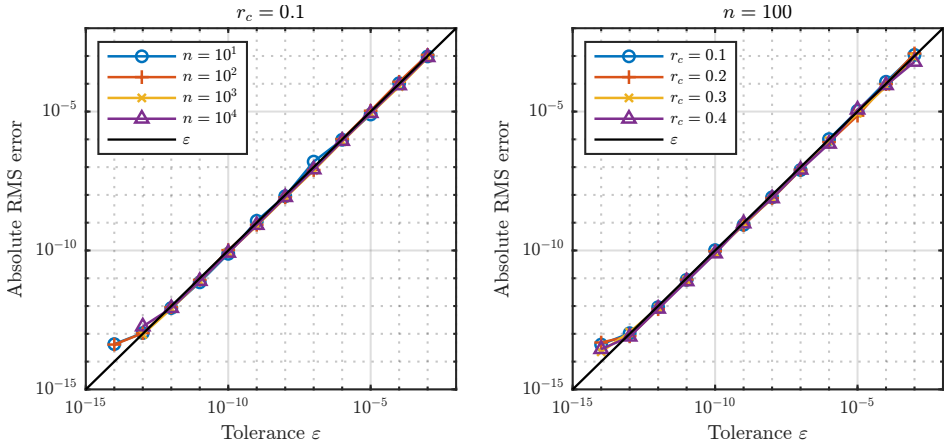


**Figure 7:** Measured absolute RMS error as a function of the requested tolerance  $\varepsilon$  for different values of  $n$  and  $r_c$ .

of strongly clustered particles, the dependence on  $n$  may therefore be more pronounced. Nevertheless, the near-collapse observed here suggests that  $C_\rho$  is close to one for the particle distributions considered in this example and that the proposed error models accurately capture the observed behavior.

Figures 5(c)–(d) further show that the truncation error scales as  $\sqrt{r_c}$ , in agreement with Proposition 1. Taken together, the results in Figure 5 confirm that the PSWF-based formulation exhibits the expected scaling behavior with respect to both the charge amplitude and the cutoff radius.

Figure 6 shows the absolute RMS error over a grid of  $(m, P)$  values. Since  $P = (2/\pi) c_w$  and  $c_s = (\pi r_c/L) m$ , the mapping  $(m, P) \mapsto (c_s, c_w)$  is linear, and the right panel therefore displays the same data as the left panel, but expressed in  $(c_s, c_w)$  coordinates. The plots demonstrate that the model (125) is in sharp agreement with the minimal  $(m, P)$  (or equivalently  $(c_s, c_w)$ ) values corresponding to each error level. The figure also includes the curves  $P = m$  and  $c_w = c_s$ , which represent simple but non-optimal choices for parameter selection.

Using the parameter selection procedure described in Algorithm 3, we aim to achieve a prescribed target accuracy for a given tolerance  $\varepsilon$ . Figure 7 shows the measured absolute RMS error plotted as functions of  $\varepsilon$ . We observe excellent agreement between the prescribed tolerance and the measured error, indicating that the parameter selection procedure performs as intended.

### 7.3.1 Comparison of PSWF/PSWF, Gaussian/PSWF, and Gaussian/Gaussian configurations

Next, we compare the errors of the PSWF/PSWF (split/window) configuration against the Gaussian/PSWF and Gaussian/Gaussian cases. All three are spectrally accurate Ewald methods with exponential convergence of the error in  $m$  and  $P$ . We treat PSWF/PSWF as our main reference; the Gaussian/PSWF comparison demonstrates the benefit of the PSWF split, while the Gaussian/Gaussian comparison provides context against the original spectral Ewald [20] configuration.

Table 3 summarizes the minimum number of Fourier modes required by each configuration to achieve prescribed target accuracies. We choose  $c_s = (r_c/\sigma)^2 = \log(1/\varepsilon)$  in order to match the truncation levels for the Gaussian and PSWF functions. We remark

**Table 3:** Resolution requirements to achieve a prescribed relative  $\ell_2$  error for Gaussian (G) and PSWF (P) splits in standard (direct) Ewald summation, and for Gaussian/Gaussian (GG), Gaussian/PSWF (GP), and PSWF/PSWF (PP) configurations in fast Ewald summation. The table reports the number of Fourier modes  $m$ , the window support  $P$ , and the cubic ratios  $(m^X/m^{PP})^3$ , where  $X \in \{G, P, GG, GP, PP\}$ . The shape parameters were chosen as  $c_s = (r_c/\sigma)^2 = \log(1/\varepsilon)$ . All results correspond to  $L = 1$ ,  $r_c = 0.1$ , and  $n = 100$ .

$\varepsilon$	$\log(\varepsilon^{-1})$	$m^G$	$m^P$	$(\frac{m^G}{m^P})^3$	$m^{GG}, P^{GG}$	$m^{GP}, P^{GP}$	$m^{PP}, P^{PP}$	$(\frac{m^{GG}}{m^{PP}})^3$	$(\frac{P^{GG}}{P^{PP}})^3$
$10^{-2}$	4.61	22	13	4.8	24, 6	24, 5	13, 5	6.3	1.7
$10^{-3}$	6.91	35	20	5.4	37, 9	35, 6	20, 6	6.3	3.4
$10^{-4}$	9.21	48	27	5.6	51, 11	52, 8	27, 8	6.7	2.6
$10^{-5}$	11.51	62	35	5.6	65, 13	66, 9	35, 9	6.7	3.0
$10^{-6}$	13.82	75	42	5.7	80, 15	79, 10	42, 10	6.9	3.4
$10^{-7}$	16.12	89	49	6.0	94, 19	94, 12	49, 12	7.1	4.0
$10^{-8}$	18.42	103	57	5.9	109, 20	109, 13	57, 13	7.0	3.6
$10^{-9}$	20.72	117	64	6.1	123, 22	123, 15	64, 15	7.1	3.2
$10^{-10}$	23.03	131	72	6.0	138, 24	138, 16	72, 16	7.0	3.4
$10^{-11}$	25.33	146	79	6.3	154, 25	154, 17	79, 17	7.4	3.2
$10^{-12}$	27.63	170	86	7.7	172, 26	172, 18	86, 18	8.0	3.0

that this parameter choice is not optimal for achieving the prescribed error tolerance without additional tuning. However, for the present test, where the goal is simply to select a reasonable shape parameter for comparison with the Gaussian case, it is perfectly adequate. In the table, we report, for each tolerance level  $\varepsilon$ , the shape parameters used, the smallest number of Fourier modes  $m$ , and the minimal window support  $P$  that satisfy the prescribed tolerance.

For the PSWF/PSWF case, the window support values  $P$  were chosen as the smallest values for which the error corresponding to a given  $c_s$  fell below the prescribed tolerance  $\varepsilon$ . This selection can be understood from Figure 4(a) by following the error curves from left to right. Owing to the presence of well-defined error plateaus, the appropriate  $P$  values in the PSWF/PSWF case are straightforward to identify. Moreover, since the same functional form governs the decay of both the split error and the windowing error, the number of Fourier modes required to achieve a given tolerance is comparable to that required by the direct Fourier sum.

For the Gaussian/Gaussian case, determining the minimal  $(m, P)$  combination is more subtle. It is well known that this algorithm does not exhibit sharply defined error plateaus, due to the nature of its approximation mechanisms, for example the use of non-truncated Gaussian functions. Consequently, the error curves transition smoothly from the exponential decay regime to the asymptotic error level, rather than displaying a clear saturation plateau. In this context, [3, 28] recommend choosing the parameters  $m$  and  $P$  slightly larger than what idealized error models would suggest. In particular, it is suggested to increase  $m$  by a factor of 1.05, a strategy that we also adopt here. This explains why the resulting  $m$  values for the Gaussian/Gaussian case are slightly larger—approximately 5%, up to rounding—than the corresponding values obtained using the direct Gaussian sum reported in the table.

Table 3 shows that the PSWF/PSWF method achieves the prescribed accuracy using both fewer Fourier modes and a smaller window support than the Gaussian/Gaussian method. In the large- $c_s$  regime, the Gaussian split requires approximately eight times as many Fourier modes as the PSWF split to reach the target tolerance for the present

configuration. As the tolerance is tightened, this ratio increases toward its asymptotic value. Taking into account the 1.05 correction factor applied to the Gaussian/Gaussian case, we estimate that the upper bound on the ratio of required Fourier modes between the Gaussian/Gaussian and PSWF/PSWF methods is approximately  $8 \times 1.05^3 \approx 9.3$ . In Table 3, the observed ratio reaches 8.0 at  $\varepsilon = 10^{-12}$ ; however, this value does not yet reflect the asymptotic limit. In addition, the required window support  $P$  is reduced by approximately a factor of three when using the PSWF window compared to the Gaussian window.

The results for the mixed Gaussian/PSWF configuration are also included in Table 3. As expected, the required Fourier resolution is comparable to that of the Gaussian/Gaussian case, while the window support is determined by—and matches—that of the PSWF window.

#### 7.4 Fast Ewald with PSWF split and B-spline window

In both the PSWF/PSWF and Gaussian/Gaussian cases, the split error and the window (aliasing) error decay exponentially fast. For the PSWF/PSWF case, we observe in Figure 4(b) that, for fixed window support  $P$ , the total error decays as  $\mathcal{O}(e^{-m})$  until it reaches the windowing error level determined by  $P$ . On a semilogarithmic scale, this behavior appears as a straight line with negative slope, which levels off into a horizontal plateau once the windowing error dominates. Although aliasing errors are formally present also for small values of  $m$ , the total error in this regime is dominated by the split truncation error. For fixed window support  $P$ , the windowing (aliasing) error is therefore essentially independent of  $m$  and determines an error floor that cannot be reduced by increasing the Fourier grid size. The same qualitative behavior is observed in the Gaussian/Gaussian case [28].

By contrast, when a B-spline window is used, the aliasing errors introduced by the windowing decay more slowly than the split errors, namely only algebraically. For fixed spline order (window support)  $P$ , the decay is typically of the form  $\mathcal{O}(m^{-P})$  [27]. As a result, the total error is eventually dominated by the windowing contribution, and, depending on the prefactor, this may occur already for relatively small values of  $m$ .

This effect is clearly illustrated in Figure 8, which shows the relative  $\ell_2$  error for the PSWF/B-spline and Gaussian/B-spline configurations. In these experiments, the split parameters are chosen as  $c_s = (r_c/\sigma)^2 = \log(1/\varepsilon)$  with  $\varepsilon = 10^{-5}$ , and B-spline orders (which coincide with the window support)  $P \in \{4, 6, 8\}$ .

In Figure 8, we observe that the error curves corresponding to the Gaussian/B-spline configuration are shifted upward relative to those of the PSWF/B-spline method. This shift is a direct consequence of the faster decay of the PSWF split error. For smaller values of  $m^3$ , the split error contributes significantly to the total error. As  $m^3$  is increased, the exponentially decaying split error becomes negligible, and the total error is instead governed by the algebraically decaying window-induced aliasing error.

To verify the algebraic convergence rate, a reference triangle is included in the plot for the case  $P = 4$ , indicating the expected slope on a log–log scale. The cases  $P = 6$  and  $P = 8$  exhibit consistent slopes, although reference triangles are omitted for clarity.

In all B-spline test cases considered here, the shape parameters were first chosen approximately at the split-error level using  $\log(1/\varepsilon)$ , so that the split error was comparable to the target tolerance. A high-resolution reference solution was then computed using direct PSWF or Gaussian summation. The error was subsequently evaluated for increasing Fourier grid sizes  $m$  until the prescribed tolerance  $\varepsilon$  was reached, at which

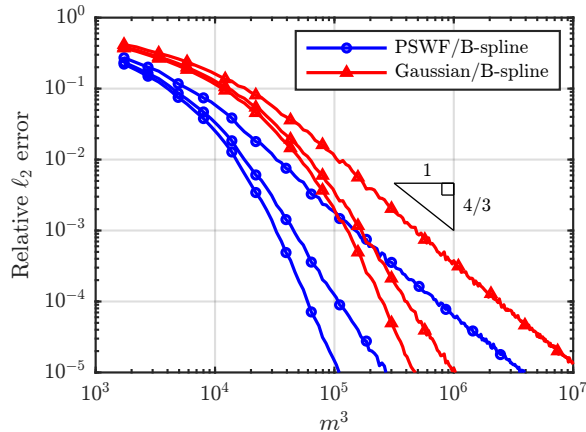


**Figure 8:** Total number of Fourier modes  $m^3$  versus relative  $\ell_2$  error for PSWF/B-spline and Gaussian/B-spline (SPME) configurations at  $L = 1$ ,  $r_c = 0.1$ ,  $n = 100$ , and B-spline order  $P \in \{4, 6, 8\}$ . The split parameters  $c_s$  (PSWF) and  $\sigma$  (Gaussian) were chosen to yield the same direct-sum split error of  $10^{-5}$ . For small and moderate  $m$ , the PSWF split yields faster error decay and reaches a given tolerance with fewer modes; for large  $m$ , both curves exhibit the same algebraic slope governed by the B-spline window. The dotted horizontal line indicates an error of  $10^{-5}$ ; the corresponding  $m$ -values where the curves cross this line are listed in Table 4.

point the corresponding value of  $m$  was recorded. One may question whether this procedure provides an appropriate basis for comparing resolution requirements, since, in the PSWF split case, the prescribed tolerance  $\varepsilon$  is often reached at values of  $m$  that are significantly smaller than those required to reduce the B-spline aliasing error to the same level. However, this behavior is precisely what motivates the chosen procedure. Increasing the PSWF bandlimit parameter  $c_s$  increases the number of Fourier modes required to reach a given tolerance, which manifests itself as an upward shift of the error curves. As a result, the minimal value of  $m$  in the PSWF/B-spline case is attained when  $c_s$  is chosen such that the split truncation error is  $\mathcal{O}(\varepsilon)$ , thereby minimizing the Fourier grid size for a fixed window support. Choosing a smaller  $c_s$  causes the split error to decay rapidly with increasing  $m$  until slowly decaying sinc-type oscillations in the PSWF spectrum dominate the total error (see Figure 1). In this regime, further reductions in  $m$  are not possible without increasing the window support. Consequently, selecting  $c_s$  so that the split error is comparable to the target tolerance yields the smallest Fourier grid size compatible with the prescribed accuracy for a fixed B-spline order, making the above procedure appropriate for assessing resolution requirements. The Gaussian (non-truncated) case is somewhat more subtle; nevertheless, we expect qualitatively similar behavior.

Table 4 summarizes the minimal values of  $m$  required to reach the tolerances  $\varepsilon \in \{10^{-2}, 10^{-3}, \dots, 10^{-6}\}$ . In practice, error tolerances in this range are typical (see, e.g., GROMACS [34]). For smaller tolerances, the use of B-spline windows becomes prohibitively expensive compared to the PSWF/PSWF and Gaussian/Gaussian configurations, and these cases are therefore omitted.

The results show that employing a PSWF split provides a clear advantage when B-spline windows are required by the implementation. Depending on the tolerance  $\varepsilon$  the number of Fourier modes is reduced by a factor of approximately 3–5 compared to the Gaussian/B-spline case, with larger improvements observed for smaller tolerances. In contrast, the Gaussian/B-spline configuration is substantially less effi-

**Table 4:** Fourier-mode requirements to achieve target tolerances  $\varepsilon \in \{10^{-2}, 10^{-3}, \dots, 10^{-6}\}$  (relative  $\ell_2$  error) for PSWF/B-spline and Gaussian/B-spline (SPME) configurations with  $L = 1$ ,  $r_c = 0.1$ ,  $n = 100$ , and B-spline orders  $P \in \{4, 6, 8\}$  (as in Figure 8). The table reports the minimum number of Fourier modes  $m$ , the cubic ratios  $(m_P^G/m_P^P)^3$  between the Gaussian/B-spline (G) and PSWF/B-spline (P) cases, and the overall ratio  $(m_P^G/m_P^{PP})^3$  relative to the PSWF/PSWF (PP) reference.

$\varepsilon$	$m_P^G$ ( $P=4, 6, 8$ )	$m_P^P$ ( $P=4, 6, 8$ )	$(m_P^G/m_P^P)^3$ ( $P=4, 6, 8$ )	$(m_P^G/m_P^{PP})^3$ ( $P=4, 6, 8$ )
$10^{-2}$	31, 25, 24	18, 15, 14	5.11, 4.63, 5.04	13.56, 7.11, 6.29
$10^{-3}$	63, 43, 39	39, 26, 23	4.22, 4.52, 4.88	31.26, 9.94, 7.41
$10^{-4}$	117, 67, 57	76, 42, 34	3.65, 4.06, 4.71	81.37, 15.28, 9.41
$10^{-5}$	230, 101, 78	154, 66, 49	3.33, 3.58, 4.03	283.78, 24.03, 11.07
$10^{-6}$	455, 156, 106	308, 100, 66	3.22, 3.80, 4.14	1271.4, 51.24, 16.08

cient than the PSWF/PSWF reference. For example, for  $P = 4$  and  $\varepsilon = 10^{-6}$ , the PSWF/PSWF method requires roughly three orders of magnitude fewer Fourier modes than the Gaussian/B-spline method, while even for  $P = 8$  a reduction by about one order of magnitude is observed at the practically relevant tolerance  $\varepsilon = 10^{-5}$ .

## 8 Conclusions

We have presented a complete description of a new version of fast Ewald summation based on the first prolate spheroidal wave function of order zero (PSWF). While PSWFs have recently attracted attention in this context, our main contribution is a systematic and unified treatment: we define PSWF-based mollifier and window functions, establish their analytical properties, and integrate them into the fast Ewald framework.

The resulting PSWF-based split has several advantageous properties. Because PSWFs form an exact Fourier transform pair on a bandlimited interval, the Fourier-space representation is particularly simple, and the residual kernel becomes compactly supported, eliminating truncation errors in the real-space sum. Consequently, the total approximation error is governed entirely by Fourier truncation and aliasing. Owing to the superior spectral localization of PSWFs, a target accuracy can be reached with substantially fewer Fourier modes and smaller window supports than in Gaussian- and B-spline-based methods. Numerical experiments confirm these predictions and show significant reductions in computational cost at fixed accuracy.

We have also derived a detailed error analysis for both Fourier truncation and window-induced aliasing. The resulting sharp bounds and simplified closed-form error models exhibit exponential decay and enable transparent and reliable parameter selection, providing a practical way to balance accuracy and efficiency.

Future work will include extending the PSWF-Ewald method and the error analysis to other interaction kernels, such as those arising in Stokes flow and wave propagation, and investigating the potential benefits of oversampling to further accelerate fast Ewald summation.

## References

- [1] L. af Klinteberg, L. Greengard, S. Jiang, and A.-K. Tornberg. Fast summation of Stokes potentials using a new kernel-splitting in the DMK framework, Sept. 2025.
- [2] L. af Klinteberg, D. S. Shamshirgar, and A.-K. Tornberg. Fast Ewald summation for free-space Stokes potentials. *Research in the Mathematical Sciences*, 4(1):1, Dec. 2017.
- [3] J. Bagge and A.-K. Tornberg. Fast Ewald summation for Stokes flow with arbitrary periodicity. *Journal of Computational Physics*, 493:112473, Nov. 2023.
- [4] A. H. Barnett. Aliasing error of the  $\exp(\beta\sqrt{1-z^2})$  kernel in the nonuniform fast fourier transform. *Applied and Computational Harmonic Analysis*, 51:1–16, Mar. 2021.
- [5] A. H. Barnett, J. Magland, and L. Af Klinteberg. A Parallel Nonuniform Fast Fourier Transform Library Based on an “Exponential of Semicircle” Kernel. *SIAM Journal on Scientific Computing*, 41(5):C479–C504, Jan. 2019.
- [6] G. Beylkin. On the Fast Fourier Transform of Functions with Singularities. *Applied and Computational Harmonic Analysis*, 2(4):363–381, Oct. 1995.
- [7] J. W. Cooley and J. W. Tukey. An Algorithm for the Machine Calculation of Complex Fourier Series. *Mathematics of Computation*, 19(90):297–301, 1965.
- [8] T. Darden, D. York, and L. Pedersen. Particle mesh Ewald: An  $N \cdot \log(N)$  method for Ewald sums in large systems. *The Journal of Chemical Physics*, 98(12):10089–10092, June 1993.
- [9] T. M. Dunster. Uniform Asymptotic Expansions for Prolate Spheroidal Functions with Large Parameters. *SIAM Journal on Mathematical Analysis*, 17(6):1495–1524, Nov. 1986.
- [10] A. Dutt and V. Rokhlin. Fast Fourier Transforms for Nonequispaced Data. *SIAM Journal on Scientific Computing*, 14(6):1368–1393, Nov. 1993.
- [11] U. Essmann, L. Perera, M. L. Berkowitz, T. Darden, H. Lee, and L. G. Pedersen. A smooth particle mesh Ewald method. *The Journal of Chemical Physics*, 103(19):8577–8593, Nov. 1995.
- [12] P. P. Ewald. Die Berechnung optischer und elektrostatischer Gitterpotentiale. *Annalen der Physik*, 369(3):253–287, 1921.
- [13] W. H. J. Fuchs. On the eigenvalues of an integral equation arising in the theory of band-limited signals. *Journal of Mathematical Analysis and Applications*, 9(3):317–330, Dec. 1964.
- [14] L. Greengard and J.-Y. Lee. Accelerating the Nonuniform Fast Fourier Transform. *SIAM Review*, 46(3):443–454, 2004.
- [15] R. W. Hockney and J. W. Eastwood. *Computer Simulation Using Particles*. CRC Press, Boca Raton, Mar. 2021.

- [16] M. Hofmann, F. Nestler, and M. Pippig. NFFT based Ewald summation for electrostatic systems with charges and dipoles. *Applied Numerical Mathematics*, 122:39–65, Dec. 2017.
- [17] S. Jiang and L. Greengard. A dual-space multilevel kernel-splitting framework for discrete and continuous convolution. *Communications on Pure and Applied Mathematics*, 2025(5):1086–1143.
- [18] J. Keiner, S. Kunis, and D. Potts. Using NFFT 3—A software library for various nonequispaced fast Fourier transforms. *ACM Transactions on Mathematical Software (TOMS)*, 36(4):1–30, 2009.
- [19] J. Liang, L. Lu, A. Barnett, L. Greengard, and S. Jiang. Accelerating Fast Ewald Summation with Prolates for Molecular Dynamics Simulations, May 2025.
- [20] D. Lindbo and A.-K. Tornberg. Spectral accuracy in fast Ewald-based methods for particle simulations. *Journal of Computational Physics*, 230(24):8744–8761, Oct. 2011.
- [21] F. Nestler. Automated parameter tuning based on RMS errors for nonequispaced FFTs. *Advances in Computational Mathematics*, 42(4):889–919, Aug. 2016.
- [22] F. Nestler, M. Pippig, and D. Potts. Fast Ewald summation based on NFFT with mixed periodicity. *Journal of Computational Physics*, 285:280–315, Mar. 2015.
- [23] A. Osipov and V. Rokhlin. On the evaluation of prolate spheroidal wave functions and associated quadrature rules. *Applied and Computational Harmonic Analysis*, 36(1):108–142, Jan. 2014.
- [24] A. Osipov, V. Rokhlin, and H. Xiao. *Prolate Spheroidal Wave Functions of Order Zero: Mathematical Tools for Bandlimited Approximation*, volume 187 of *Applied Mathematical Sciences*. Springer US, Boston, MA, 2013.
- [25] G. Plonka, D. Potts, G. Steidl, and M. Tasche. *Numerical Fourier Analysis*. Applied and Numerical Harmonic Analysis. Springer International Publishing, Cham, 2018.
- [26] D. Potts, G. Steidl, and M. Tasche. Fast Fourier Transforms for Nonequispaced Data: A Tutorial. In J. J. Benedetto and P. J. S. G. Ferreira, editors, *Modern Sampling Theory: Mathematics and Applications*, pages 247–270. Birkhäuser, Boston, MA, 2001.
- [27] I. J. Schoenberg. *Cardinal Spline Interpolation*. Society for Industrial and Applied Mathematics, Jan. 1973.
- [28] D. S. Shamshirgar, J. Bagge, and A.-K. Tornberg. Fast Ewald summation for electrostatic potentials with arbitrary periodicity. *The Journal of Chemical Physics*, 154(16):164109, Apr. 2021.
- [29] D. Slepian. Some Asymptotic Expansions for Prolate Spheroidal Wave Functions. *Journal of Mathematics and Physics*, 44(1-4):99–140, Apr. 1965.
- [30] D. Slepian. Some comments on Fourier analysis, uncertainty and modeling. *SIAM Review*, 25(3):379–393, July 1983.

- [31] D. Slepian and H. O. Pollak. Prolate Spheroidal Wave Functions, Fourier Analysis and Uncertainty - I. *Bell System Technical Journal*, 40(1):43–63, Jan. 1961.
- [32] G. Steidl. A note on fast Fourier transforms for nonequispaced grids. *Advances in Computational Mathematics*, 9(3):337–352, Nov. 1998.
- [33] T. A. Driscoll, N. Hale, and L. N. Trefethen, editors. *Chebfun Guide*, volume 2014. Pafnuty Publications, Oxford.
- [34] D. Van Der Spoel, E. Lindahl, B. Hess, G. Groenhof, A. E. Mark, and H. J. C. Berendsen. GROMACS: Fast, flexible, and free. *Journal of Computational Chemistry*, 26(16):1701–1718, Dec. 2005.

## A PSWF asymptotics and approximations

In this section, we present the asymptotic behavior of  $\psi_0^c$ , along with corresponding approximations. These results are used to derive the closed-form approximations in Section 5.

Considering the Fourier tail behavior, the PSWF scaling (see Theorem 1) yields

$$1 - \mu_0(c) = 2\pi \int_{\mathbb{R} \setminus [-c, c]} |\widehat{\psi}_0^c(\omega)|^2 d\omega = \|\widehat{\psi}_0^c\|_{L^2(\mathbb{R} \setminus [-c, c])}^2, \quad (131)$$

where  $\mu_0(c) = c/(2\pi) \lambda_0^2$  is the first concentration eigenvalue associated with  $\psi_0^c$  and  $\|\psi_0^c\|_{L^2(-1,1)} = 1$ . Fuchs [13] proved the asymptotic behaviour

$$1 - \mu_0(c) \sim 4\sqrt{\pi c} e^{-2c} \quad \text{as } c \rightarrow \infty, \quad (132)$$

and therefore

$$\|\widehat{\psi}_0^c\|_{L^2(\mathbb{R} \setminus [-c, c])} \sim C_F c^{1/4} e^{-c}, \quad (133)$$

where the constant  $C_F > 0$  depends on the chosen Fourier-transform convention.

For large  $c$ , the first PSWF eigenvalue of the differential operator satisfies [24]

$$\lambda_0(c) \sim \sqrt{\frac{2\pi}{c}}. \quad (134)$$

The Fourier–eigenfunction identity at the end-points (Lemma 2)

$$\widehat{\psi}_0^c(c) = \lambda_0(c) \psi_0^c(1) \quad (135)$$

shows that the decay of  $\widehat{\psi}_0^c(c)$  determines the decay of  $\psi_0^c(1)$ . Using (134) and (135) gives

$$\frac{\psi_0^c(1)}{\psi_0^c(0)} \sim \sqrt{\frac{c}{2\pi}} \frac{\widehat{\psi}_0^c(c)}{\widehat{\psi}_0^c(0)}. \quad (136)$$

Motivated by the strong exponential localization of  $\widehat{\psi}_0^c$  near  $|\omega| = c$ , we approximate

$$\widehat{\psi}_0^c(c) \sim \|\widehat{\psi}_0^c\|_{L^2(\mathbb{R} \setminus [-c, c])}. \quad (137)$$

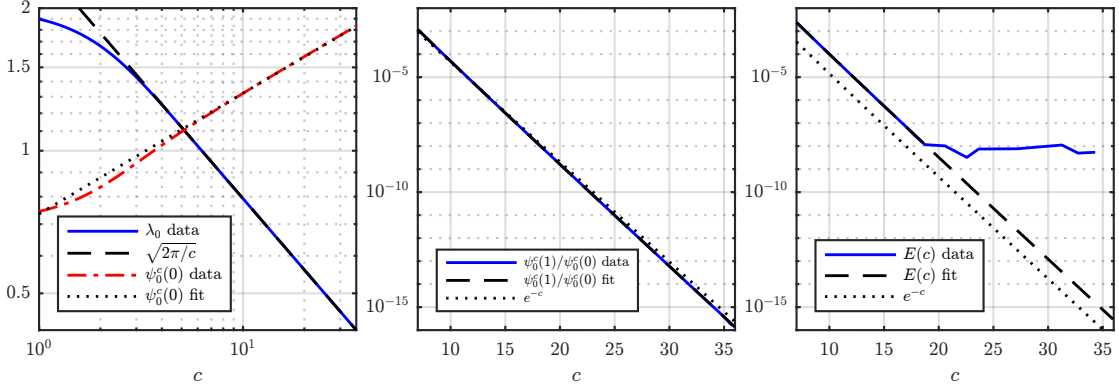


**Figure 9:** Curve-fitted approximations of key PSWF quantities;  $E(c) := \frac{2}{c \psi_0^c(0)} \sqrt{\frac{2\pi}{\lambda_0^2} - c}$ .

Furthermore, it is well known from WKB analysis of the PSWF equation (see Dunster [9]) that

$$\psi_0^c(0) \sim C_0 c^{1/4}. \quad (138)$$

Based on the relations above, we fit the following expressions numerically in the interval  $7 \leq c \leq 35$ :

$$\lambda_0 \approx \sqrt{\frac{2\pi}{c}}, \quad (139)$$

$$\psi_0^c(0) \approx A_0 c^{1/4}, \quad (140)$$

$$\psi_0^c(1) \approx A_1 c^{3/4} e^{-c}, \quad (141)$$

$$\frac{\psi_0^c(1)}{\psi_0^c(0)} \approx A_2 c^{1/2} e^{-c}, \quad (142)$$

$$\frac{2}{c \psi_0^c(0)} \sqrt{\frac{2\pi}{\lambda_0^2} - c} \approx A_3 c^{-1/2} e^{-c}. \quad (143)$$

Here, (141) is obtained from (136) together with (133) and (138), and the expression for  $\psi_0^c(1)$  follows from multiplying (142) by (140). The expression in (143) is fitted with an exponential, motivated by (132):

$$\frac{2}{c \psi_0^c(0)} \sqrt{\frac{2\pi}{\lambda_0^2} - c} = \frac{2\sqrt{c}}{c \psi_0^c(0) \sqrt{\mu_0(c)}} \sqrt{1 - \mu_0(c)} \sim C c^{-1/2} e^{-c}. \quad (144)$$

The results are presented in Table 5 and Figure 9. For all expressions, it is possible to obtain a fit with maximum relative errors of about 1%. If the lower bound of the fitting interval is increased above  $c = 7$ , the fit typically improves further.

The upper limit  $c \lesssim 35$  is chosen because the numerical evaluation of  $\psi_0^c$  approaches machine precision beyond this point.

## B Numerical evaluation of $\psi_0^c$ and $(\psi_0^c)'$

The numerical evaluation of  $\psi_0^c$  we propose follows the algorithmic framework of Osipov and Rokhlin [23]. A short summary is given below.

**Table 5:** Curve-fitted models together with fit quality for  $7 \leq c \leq 35$ .

Quantity	Model	Max rel. error
$\lambda_0(c)$	$\sqrt{2\pi/c}$	< 0.1% at $c = 7$
$\psi_0^c(0)$	$0.736 c^{0.2548}$	$\approx 0.4\%$ at $c = 7$
$\psi_0^c(1)$	$2.540 c^{3/4} e^{-c}$	$\approx 1.6\%$ at $c = 7$
$\psi_0^c(1)/\psi_0^c(0)$	$3.424 c^{1/2} e^{-c}$	$\approx 1.5\%$ at $c = 35$
$\frac{2}{c\psi_0^c(0)} \sqrt{\frac{2\pi}{\lambda_0^2} - c}$	$6.906 c^{-1/2} e^{-c}$	$\approx 0.2\%$ at $c = 7$

## B.1 Legendre expansion and eigenproblem

The function  $\psi_0^c$  is represented as

$$\psi_0^c(x) = \sum_{k=0}^K a_{2k} P_{2k}(x), \quad (145)$$

where only even Legendre polynomials appear due to symmetry. Here  $P_k$  denotes the standard (unnormalized) Legendre polynomial; the normalized basis  $\bar{P}_k(x) = \sqrt{k + \frac{1}{2}} P_k(x)$  used in [23] leads to an equivalent eigenproblem with rescaled coefficients. Substitution into the differential equation

$$\frac{d}{dx} \left( (1 - x^2) \psi'(x) \right) + (\chi_0 - c^2 x^2) \psi(x) = 0 \quad (146)$$

leads to a three-term recurrence for the coefficients  $\{a_{2k}\}$ . After truncation at order  $K$ , a finite-dimensional symmetric tridiagonal eigenproblem is obtained. Its smallest eigenvalue corresponds to  $\chi_0$  and the associated eigenvector provides the coefficients  $a_{2k}$  [23, Theorem 10].

## B.2 Computation of eigenpairs

The tridiagonal structure permits efficient and accurate computation of the eigenvalue  $\chi_0$  and the coefficient vector  $\{a_{2k}\}$ . In practice, Sturm bisection followed by inverse iteration is applied, as recommended in [23, Sec. 3.4]. This yields rapidly convergent approximations to  $\psi_0^c$  with complexity  $\mathcal{O}(K^2)$ .

## B.3 Evaluation of $\psi_0^c$ and $\lambda_0$

Once the Legendre coefficients are available,  $\psi_0^c$  is evaluated directly from its expansion. The eigenvalue  $\lambda_0(c)$  of the integral operator is then obtained from

$$\lambda_0 = \frac{1}{\psi_0^c(0)} \int_{-1}^1 \psi_0^c(s) ds, \quad (147)$$

using high-order Gauss–Legendre quadrature [23, Sec. 3.2].

## B.4 Evaluation of $(\psi_0^c)'$

Given the Legendre expansion (145) the derivative can be computed as

$$(\psi_0^c)'(x) = \sum_{k=0}^K a_{2k} P'_{2k}(x). \quad (148)$$

Another way is to differentiate (23) and evaluate the following integral using a numerical quadrature:

$$(\psi_0^c)'(x) = \frac{ic}{\lambda_0} \int_{-1}^1 t \psi_0^c(t) e^{icxt} dt. \quad (149)$$

## B.5 Truncation order

The required number of terms  $K$  in the expansion grows linearly with the bandlimit  $c$ . Empirically,  $K \approx 1.2c$  suffices to achieve  $10^{-12}$  accuracy, in agreement with the decay estimates for the Legendre coefficients in [23, Remark 9].

## C Auxiliary standard results

### C.1 Radial extension (Fourier-side definition)

Let  $f : \mathbb{R} \rightarrow \mathbb{R}$  be even and belong to  $L^1(\mathbb{R})$ , with Fourier transform  $\hat{f}$ . Define the radially symmetric function  $\eta : \mathbb{R}^3 \rightarrow \mathbb{R}$  by

$$\widehat{\eta}(\boldsymbol{\omega}) := \hat{f}(|\boldsymbol{\omega}|), \quad \boldsymbol{\omega} \in \mathbb{R}^3. \quad (150)$$

Equivalently, in physical space,

$$\eta(\mathbf{x}) = \frac{1}{2\pi^2} \int_0^\infty \hat{f}(\rho) \frac{\sin(\rho|\mathbf{x}|)}{\rho|\mathbf{x}|} \rho^2 d\rho. \quad (151)$$

**Remark 15.** *In general,  $\eta(\mathbf{x}) \neq f(|\mathbf{x}|)$ ; the identification is through the three-dimensional radial (spherical Bessel) integral above, not by pointwise substitution.*

### C.2 Derivation of (19)

For completeness, we provide the standard calculation leading to (19). Starting from the definition of the Fourier coefficients of the periodized function  $\tilde{f}$ ,

$$c_{\mathbf{k}}(\tilde{f}) = \frac{1}{V} \int_{\Omega} \tilde{f}(\mathbf{x}) e^{-\frac{2\pi i}{L} \mathbf{k} \cdot \mathbf{x}} d\mathbf{x}, \quad (152)$$

and substituting the definition of  $\tilde{f}$ , we obtain

$$\begin{aligned} c_{\mathbf{k}}(\tilde{f}) &= \frac{1}{V} \int_{\Omega} \sum_{\mathbf{r} \in \mathbb{Z}^3} f(\mathbf{x} + L\mathbf{r}) e^{-\frac{2\pi i}{L} \mathbf{k} \cdot \mathbf{x}} d\mathbf{x} \\ &= \frac{1}{V} \sum_{\mathbf{r} \in \mathbb{Z}^3} \int_{\Omega + L\mathbf{r}} f(\mathbf{x}) e^{-\frac{2\pi i}{L} \mathbf{k} \cdot (\mathbf{x} - L\mathbf{r})} d\mathbf{x} \\ &= \frac{1}{V} \int_{\mathbb{R}^3} f(\mathbf{x}) e^{-\frac{2\pi i}{L} \mathbf{k} \cdot \mathbf{x}} d\mathbf{x}, \quad \text{since } e^{2\pi i \mathbf{k} \cdot \mathbf{r}} = 1, \\ &= \frac{1}{V} \widehat{f}(\mathbf{k}). \end{aligned} \quad (153)$$

### C.3 A lattice-to-continuum estimate

We recall a standard lattice covering argument that bounds radial lattice sums by corresponding integrals. This estimate is used in the proof of Lemma 4 to pass from discrete sums to radial integrals.

**Lemma 6** (Lattice covering lemma in  $\mathbb{R}^3$ ). *Let  $f : [0, \infty) \rightarrow [0, \infty)$  be nonincreasing. For  $K > \sqrt{3}/2$ ,*

$$\sum_{|\mathbf{k}|>K} f(|\mathbf{k}|) \leq \int_{|\mathbf{x}|>K-\sqrt{3}/2} f(|\mathbf{x}|) d\mathbf{x}. \quad (154)$$

*Proof.* Partition  $\mathbb{R}^3$  into cubes  $Q_{\mathbf{k}} = \mathbf{k} + [-\frac{1}{2}, \frac{1}{2})^3$ . For any  $\mathbf{x} \in Q_{\mathbf{k}}$  one has  $||\mathbf{x}| - |\mathbf{k}|| \leq \sqrt{3}/2$ . Monotonicity of  $f$  then yields the stated bound.  $\square$